



<b>Publication Year</b>	2016
<b>Acceptance in OA</b>	2020-05-15T08:26:18Z
<b>Title</b>	Fermi-LAT Observations of High-Energy Gamma-Ray Emission toward the Galactic Center
<b>Authors</b>	Ajello, M., Albert, A., Atwood, W. B., Barbiellini, G., Bastieri, D., Bechtol, K., Bellazzini, R., Bissaldi, E., Blandford, R. D., Bloom, E. D., Bonino, R., Bottacini, E., Brandt, T. J., Bregeon, J., Bruel, P., Buehler, R., Buson, S., Caliendo, G. A., Cameron, R. A., Caputo, R., Caragiulo, M., CARAVEO, PATRIZIA, Cecchi, C., Chekhtman, A., Chiang, J., Chiaro, G., Ciprini, S., Cohen-Tanugi, J., Cominsky, L. R., Conrad, J., Cutini, S., D'AMMANDO, FILIPPO, de Angelis, A., de Palma, F., Desiante, R., Di Venere, L., Drell, P. S., Favuzzi, C., Ferrara, E. C., Fusco, P., Gargano, F., Gasparrini, D., Giglietto, N., Giommi, P., Giordano, F., GIROLETTI, MARCELLO, Glanzman, T., Godfrey, G., Gomez-Vargas, G. A., Grenier, I. A., Guiriec, S., Gustafsson, M., Harding, A. K., Hewitt, J. W., Hill, A. B., Horan, D., Jogler, T., Jóhannesson, G., Johnson, A. S., Kamae, T., Karwin, C., Knödlseeder, J., Kuss, M., Larsson, S., Latronico, L., Li, J., Li, L., Longo, F., Loparco, F., Lovellette, M. N., Lubrano, P., Magill, J., Maldera, S., Malyshev, D., Manfreda, A., Mayer, M., Mazziotta, M. N., Michelson, P. F., Mitthumsiri, W., Mizuno, T., Moiseev, A. A., Monzani, M. E., Morselli, A., Moskalenko, I. V., Murgia, S., Nuss, E., Ohno, M., Ohsugi, T., Omodei, N., Orlando, E., Ormes, J. F., Paneque, D., Pesce-Rollins, M., Piron, F., Pivato, G., Porter, T. A., Rainò, S., Rando, R., Razzano, M., Reimer, A., Reimer, O., Ritz, S., Sánchez-Conde, M., Saz Parkinson, P. M., Sgrò, C., Siskind, E. J., Smith, D. A., Spada, F., Spandre, G., Spinelli, P., Suson, D. J., Tajima, H., Takahashi, H., Thayer, J. B., Torres, D. F., Tosti, G., Troja, E., Uchiyama, Y., Vianello, G., Winer, B. L., Wood, K. S., Zaharijas, G., Zimmer, S.
<b>Publisher's version (DOI)</b>	10.3847/0004-637X/819/1/44
<b>Handle</b>	<a href="http://hdl.handle.net/20.500.12386/24854">http://hdl.handle.net/20.500.12386/24854</a>
<b>Journal</b>	THE ASTROPHYSICAL JOURNAL
<b>Volume</b>	819



## FERMI-LAT OBSERVATIONS OF HIGH-ENERGY $\gamma$ -RAY EMISSION TOWARD THE GALACTIC CENTER

M. AJELLO<sup>1</sup>, A. ALBERT<sup>2</sup>, W. B. ATWOOD<sup>3</sup>, G. BARBIELLINI<sup>4,5</sup>, D. BASTIERI<sup>6,7</sup>, K. BECHTOL<sup>8</sup>, R. BELLAZZINI<sup>9</sup>, E. BISSALDI<sup>10</sup>, R. D. BLANDFORD<sup>2</sup>, E. D. BLOOM<sup>2</sup>, R. BONINO<sup>11,12</sup>, E. BOTTACINI<sup>2</sup>, T. J. BRANDT<sup>13</sup>, J. BREGEON<sup>14</sup>, P. BRUEL<sup>15</sup>, R. BUEHLER<sup>16</sup>, S. BUSON<sup>6,7</sup>, G. A. CALIANDRO<sup>2,17</sup>, R. A. CAMERON<sup>2</sup>, R. CAPUTO<sup>3</sup>, M. CARAGIULO<sup>10</sup>, P. A. CARAVEO<sup>18</sup>, C. CECCHI<sup>19,20</sup>, A. CHEKHTMAN<sup>21,64</sup>, J. CHIANG<sup>2</sup>, G. CHIARO<sup>7</sup>, S. CIPRINI<sup>19,22,23</sup>, J. COHEN-TANUGI<sup>14</sup>, L. R. COMINSKY<sup>24</sup>, J. CONRAD<sup>25,26,27</sup>, S. CUTINI<sup>19,22,23</sup>, F. D'AMMANDO<sup>28,29</sup>, A. DE ANGELIS<sup>30</sup>, F. DE PALMA<sup>10,31</sup>, R. DESIANTE<sup>11,32</sup>, L. DI VENERE<sup>33</sup>, P. S. DRELL<sup>2</sup>, C. FAVUZZI<sup>10,33</sup>, E. C. FERRARA<sup>13</sup>, P. FUSCO<sup>10,33</sup>, F. GARGANO<sup>10</sup>, D. GASPARRINI<sup>19,22,23</sup>, N. GIGLIETTO<sup>10,33</sup>, P. GIOMMI<sup>22</sup>, F. GIORDANO<sup>10,33</sup>, M. GIROLETTI<sup>28</sup>, T. GLANZMAN<sup>2</sup>, G. GODFREY<sup>2</sup>, G. A. GOMEZ-VARGAS<sup>34,35</sup>, I. A. GRENIER<sup>36</sup>, S. GUIRIEC<sup>13</sup>, M. GUSTAFSSON<sup>37</sup>, A. K. HARDING<sup>13</sup>, J. W. HEWITT<sup>38</sup>, A. B. HILL<sup>2,39</sup>, D. HORAN<sup>15</sup>, T. JOGLER<sup>2</sup>, G. JÓHANNESSEN<sup>40</sup>, A. S. JOHNSON<sup>2</sup>, T. KAMAE<sup>41</sup>, C. KARWIN<sup>42</sup>, J. KNÖDLSEDER<sup>43,44</sup>, M. KUSS<sup>9</sup>, S. LARSSON<sup>26,45</sup>, L. LATRONICO<sup>11</sup>, J. LI<sup>46</sup>, L. LI<sup>26,45</sup>, F. LONGO<sup>4,5</sup>, F. LOPARCO<sup>10,33</sup>, M. N. LOVELLETTE<sup>47</sup>, P. LUBRANO<sup>19,20</sup>, J. MAGILL<sup>48</sup>, S. MALDERA<sup>11</sup>, D. MALYSHEV<sup>2</sup>, A. MANFREDA<sup>9</sup>, M. MAYER<sup>16</sup>, M. N. MAZZIOTTA<sup>10</sup>, P. F. MICHELSON<sup>2</sup>, W. MITTHUMSIRI<sup>49</sup>, T. MIZUNO<sup>50</sup>, A. A. MOISEEV<sup>48,51</sup>, M. E. MONZANI<sup>2</sup>, A. MORSELLI<sup>34</sup>, I. V. MOSKALENKO<sup>2</sup>, S. MURGIA<sup>42</sup>, E. NUSS<sup>14</sup>, M. OHNO<sup>52</sup>, T. OHSUGI<sup>50</sup>, N. OMODEI<sup>2</sup>, E. ORLANDO<sup>2</sup>, J. F. ORMES<sup>53</sup>, D. PANEQUE<sup>2,69</sup>, M. PESCE-ROLLINS<sup>2,9</sup>, F. PIRON<sup>14</sup>, G. PIVATO<sup>9</sup>, T. A. PORTER<sup>2</sup>, S. RAINÒ<sup>10,33</sup>, R. RANDO<sup>6,7</sup>, M. RAZZANO<sup>9</sup>, A. REIMER<sup>2,63</sup>, O. REIMER<sup>2,63</sup>, S. RITZ<sup>3</sup>, M. SÁNCHEZ-CONDE<sup>25,26</sup>, P. M. SAZ PARKINSON<sup>3,54</sup>, C. SGRÒ<sup>9</sup>, E. J. SISKIND<sup>55,56</sup>, D. A. SMITH<sup>57</sup>, F. SPADA<sup>9</sup>, G. SPANDRE<sup>9</sup>, P. SPINELLI<sup>10,33</sup>, D. J. SUSON<sup>58</sup>, H. TAJIMA<sup>2,59</sup>, H. TAKAHASHI<sup>52</sup>, J. B. THAYER<sup>2</sup>, D. F. TORRES<sup>46,60</sup>, G. TOSTI<sup>19,20</sup>, E. TROJA<sup>13,48</sup>, Y. UCHIYAMA<sup>61</sup>, G. VIANELLO<sup>2</sup>, B. L. WINER<sup>62</sup>, K. S. WOOD<sup>47</sup>, G. ZAHARIJAS<sup>4,5</sup>, AND S. ZIMMER<sup>25,26</sup>

<sup>1</sup> Department of Physics and Astronomy, Clemson University, Kinard Lab of Physics, Clemson, SC 29634-0978, USA

<sup>2</sup> W. W. Hansen Experimental Physics Laboratory, Kavli Institute for Particle Astrophysics and Cosmology, Department of Physics and SLAC National Accelerator Laboratory, Stanford University, Stanford, CA 94305, USA; [tporter@stanford.edu](mailto:tporter@stanford.edu)

<sup>3</sup> Santa Cruz Institute for Particle Physics, Department of Physics and Department of Astronomy and Astrophysics, University of California at Santa Cruz, Santa Cruz, CA 95064, USA

<sup>4</sup> Istituto Nazionale di Fisica Nucleare, Sezione di Trieste, I-34127 Trieste, Italy

<sup>5</sup> Dipartimento di Fisica, Università di Trieste, I-34127 Trieste, Italy

<sup>6</sup> Istituto Nazionale di Fisica Nucleare, Sezione di Padova, I-35131 Padova, Italy

<sup>7</sup> Dipartimento di Fisica e Astronomia "G. Galilei," Università di Padova, I-35131 Padova, Italy

<sup>8</sup> Dept. of Physics and Wisconsin IceCube Particle Astrophysics Center, University of Wisconsin, Madison, WI 53706, USA

<sup>9</sup> Istituto Nazionale di Fisica Nucleare, Sezione di Pisa, I-56127 Pisa, Italy

<sup>10</sup> Istituto Nazionale di Fisica Nucleare, Sezione di Bari, I-70126 Bari, Italy

<sup>11</sup> Istituto Nazionale di Fisica Nucleare, Sezione di Torino, I-10125 Torino, Italy

<sup>12</sup> Dipartimento di Fisica Generale "Amadeo Avogadro," Università degli Studi di Torino, I-10125 Torino, Italy

<sup>13</sup> NASA Goddard Space Flight Center, Greenbelt, MD 20771, USA

<sup>14</sup> Laboratoire Univers et Particules de Montpellier, Université Montpellier, CNRS/IN2P3, Montpellier, France

<sup>15</sup> Laboratoire Leprince-Ringuet, École polytechnique, CNRS/IN2P3, Palaiseau, France

<sup>16</sup> Deutsches Elektronen Synchrotron DESY, D-15738 Zeuthen, Germany

<sup>17</sup> Consorzio Interuniversitario per la Fisica Spaziale (CIFS), I-10133 Torino, Italy

<sup>18</sup> INFN-Istituto di Astrofisica Spaziale e Fisica Cosmica, I-20133 Milano, Italy

<sup>19</sup> Istituto Nazionale di Fisica Nucleare, Sezione di Perugia, I-06123 Perugia, Italy

<sup>20</sup> Dipartimento di Fisica, Università degli Studi di Perugia, I-06123 Perugia, Italy

<sup>21</sup> College of Science, George Mason University, Fairfax, VA 22030, USA

<sup>22</sup> Agenzia Spaziale Italiana (ASI) Science Data Center, I-00133 Roma, Italy

<sup>23</sup> INFN Osservatorio Astronomico di Roma, I-00040 Monte Porzio Catone (Roma), Italy

<sup>24</sup> Department of Physics and Astronomy, Sonoma State University, Rohnert Park, CA 94928-3609, USA

<sup>25</sup> Department of Physics, Stockholm University, AlbaNova, SE-106 91 Stockholm, Sweden

<sup>26</sup> The Oskar Klein Centre for Cosmoparticle Physics, AlbaNova, SE-106 91 Stockholm, Sweden

<sup>27</sup> The Royal Swedish Academy of Sciences, Box 50005, SE-104 05 Stockholm, Sweden

<sup>28</sup> INFN Istituto di Radioastronomia, I-40129 Bologna, Italy

<sup>29</sup> Dipartimento di Astronomia, Università di Bologna, I-40127 Bologna, Italy

<sup>30</sup> Dipartimento di Fisica, Università di Udine and Istituto Nazionale di Fisica Nucleare, Sezione di Trieste, Gruppo Collegato di Udine, I-33100 Udine

<sup>31</sup> Università Telematica Pegaso, Piazza Trieste e Trento, 48, I-80132 Napoli, Italy

<sup>32</sup> Università di Udine, I-33100 Udine, Italy

<sup>33</sup> Dipartimento di Fisica "M. Merlin" dell'Università e del Politecnico di Bari, I-70126 Bari, Italy

<sup>34</sup> Istituto Nazionale di Fisica Nucleare, Sezione di Roma "Tor Vergata," I-00133 Roma, Italy

<sup>35</sup> Departamento de Física, Pontificia Universidad Católica de Chile, Avenida Vicuña Mackenna 4860, Santiago, Chile

<sup>36</sup> Laboratoire AIM, CEA-IRFU/CNRS/Université Paris Diderot, Service d'Astrophysique, CEA Saclay, F-91191 Gif sur Yvette, France

<sup>37</sup> Georg-August University Göttingen, Institute for theoretical Physics—Faculty of Physics, Friedrich-Hund-Platz 1, D-37077 Göttingen, Germany

<sup>38</sup> University of North Florida, Department of Physics, 1 UNF Drive, Jacksonville, FL 32224, USA

<sup>39</sup> School of Physics and Astronomy, University of Southampton, Highfield, Southampton, SO17 1BJ, UK

<sup>40</sup> Science Institute, University of Iceland, IS-107 Reykjavik, Iceland

<sup>41</sup> Department of Physics, Graduate School of Science, University of Tokyo, 7-3-1 Hongo, Bunkyo-ku, Tokyo 113-0033, Japan

<sup>42</sup> Center for Cosmology, Physics and Astronomy Department, University of California, Irvine, CA 92697-2575, USA; [smurgia@uci.edu](mailto:smurgia@uci.edu)

<sup>43</sup> CNRS, IRAP, F-31028 Toulouse cedex 4, France

<sup>44</sup> GAHEC, Université de Toulouse, UPS-OMP, IRAP, Toulouse, France

<sup>45</sup> Department of Physics, KTH Royal Institute of Technology, AlbaNova, SE-106 91 Stockholm, Sweden

<sup>46</sup> Institute of Space Sciences (IEEC-CSIC), Campus UAB, E-08193 Barcelona, Spain

<sup>47</sup> Space Science Division, Naval Research Laboratory, Washington, DC 20375-5352, USA

<sup>48</sup> Department of Physics and Department of Astronomy, University of Maryland, College Park, MD 20742, USA

<sup>49</sup> Department of Physics, Faculty of Science, Mahidol University, Bangkok 10400, Thailand

<sup>50</sup> Hiroshima Astrophysical Science Center, Hiroshima University, Higashi-Hiroshima, Hiroshima 739-8526, Japan

<sup>51</sup> Center for Research and Exploration in Space Science and Technology (CRESST) and NASA Goddard Space Flight Center, Greenbelt, MD 20771, USA

<sup>52</sup> Department of Physics and Astronomy, University of Denver, Denver, CO 80208, USA

<sup>53</sup> Max-Planck-Institut für Physik, D-80805 München, Germany

<sup>54</sup> Department of Physics, The University of Hong Kong, Pokfulam Road, Hong Kong, China

<sup>55</sup> NYCB Real-Time Computing Inc., Lattingtown, NY 11560-1025, USA

<sup>56</sup> Department of Chemistry and Physics, Purdue University Calumet, Hammond, IN 46323-2094, USA

<sup>57</sup> Solar-Terrestrial Environment Laboratory, Nagoya University, Nagoya 464-8601, Japan

<sup>58</sup> Institució Catalana de Recerca i Estudis Avançats (ICREA), Barcelona, Spain

<sup>59</sup> 3-34-1 Nishi-Ikebukuro, Toshima-ku, Tokyo 171-8501, Japan

<sup>60</sup> Department of Physics, Center for Cosmology and Astro-Particle Physics, The Ohio State University, Columbus, OH 43210, USA

<sup>61</sup> Istituto Nazionale di Fisica Nucleare, Sezione di Trieste, and Università di Trieste, I-34127 Trieste, Italy

<sup>62</sup> Laboratory for Astroparticle Physics, University of Nova Gorica, Vipavska 13, SI-5000 Nova Gorica, Slovenia

<sup>63</sup> Institut für Astro- und Teilchenphysik and Institut für Theoretische Physik, Leopold-Franzens-Universität Innsbruck, A-6020 Innsbruck, Austria

Received 2015 September 5; accepted 2015 November 25; published 2016 February 26

## ABSTRACT

The *Fermi* Large Area Telescope (LAT) has provided the most detailed view to date of the emission toward the Galactic center (GC) in high-energy  $\gamma$ -rays. This paper describes the analysis of data taken during the first 62 months of the mission in the energy range 1–100 GeV from a  $15^\circ \times 15^\circ$  region about the direction of the GC. Specialized interstellar emission models (IEMs) are constructed to enable the separation of the  $\gamma$ -ray emissions produced by cosmic ray particles interacting with the interstellar gas and radiation fields in the Milky Way into that from the inner  $\sim 1$  kpc surrounding the GC, and that from the rest of the Galaxy. A catalog of point sources for the  $15^\circ \times 15^\circ$  region is self-consistently constructed using these IEMs: the First *Fermi*-LAT Inner Galaxy Point Source Catalog (1FIG). The spatial locations, fluxes, and spectral properties of the 1FIG sources are presented, and compared with  $\gamma$ -ray point sources over the same region taken from existing catalogs. After subtracting the interstellar emission and point-source contributions a residual is found. If templates that peak toward the GC are used to model the positive residual the agreement with the data improves, but none of the additional templates tried account for all of its spatial structure. The spectrum of the positive residual modeled with these templates has a strong dependence on the choice of IEM.

**Key words:** cosmic rays – Galaxy: center – gamma-rays: general – gamma-rays: ISM – radiation mechanisms: non-thermal

## 1. INTRODUCTION

The region surrounding the Galactic center (GC) is among the brightest and most complex in high-energy  $\gamma$ -rays, with on-going massive star formation providing all types of known or suspected cosmic ray (CR) and  $\gamma$ -ray sources. The GC also houses a  $\sim 10^6 M_\odot$  black hole (e.g., Genzel et al. 2010) and the region is predicted to be the brightest source of  $\gamma$ -rays associated with annihilation or decay of massive weakly interacting particles (see the reviews by, e.g., Jungman et al. 1996; Bergström 2000; Feng 2010). Despite detection in the 100 MeV to GeV range by the EGRET instrument on the *Compton Gamma-ray Observatory* (Mayer-Hasselwander et al. 1998) and at higher energies by the H.E.S.S. Cherenkov array (Aharonian et al. 2006a, 2006b) the characterization of the  $\gamma$ -ray emission for  $< 100$  GeV energies in the region surrounding the GC has remained elusive.

The  $\gamma$ -ray emission in the Galaxy is predominantly due to the interactions of CR particles with the interstellar gas and radiation fields. This interstellar emission is a fore-/background against which  $\gamma$ -ray point sources are detected. In the Galactic plane the intensity of this emission makes disentangling the contributions by  $\gamma$ -ray point sources and truly diffuse processes challenging. Particularly toward the GC, where the intensity of the interstellar emission and number

of point sources is maximized, self-consistent modeling is necessary to deal with the strong confusion.

Since 2008 the Large Area Telescope instrument on the *Fermi* Gamma-Ray Space Telescope (*Fermi*-LAT) has been taking data in the range 20 MeV to more than 300 GeV energies. Analyses of the data toward the region surrounding the GC have been made by various authors (Goodenough & Hooper 2009; Hooper & Goodenough 2011; Abazajian & Kaplinghat 2012; Gordon & Macías 2013; Hooper & Slatyer 2013; Huang et al. 2013; Abazajian et al. 2014; Daylan et al. 2014; Calore et al. 2015a). The results of these works have been interpreted as evidence for an unresolved point source population or annihilating dark matter (DM). Versions of the interstellar emission models (IEMs) distributed by the *Fermi* Science Support Center (FSSC)<sup>65</sup> have typically been employed in these analyses, although some works have used IEMs (e.g., Calore et al. 2015a) that are based on CR propagation calculations using the GALPROP code<sup>66</sup> (e.g., Moskalenko & Strong 1998; Vladimirov et al. 2012).

The FSSC IEMs are optimized to flatten residuals over large regions of the sky in support of the generation of the *Fermi*-LAT source catalogs. The optimizations vary according to the version of the FSSC IEM. The most widely used by the analyses cited above (supporting the generation of the Second *Fermi*-LAT Source Catalog; Nolan et al. 2012) includes

<sup>64</sup> Funded by contract FIRB-2012-RBFR12PM1F from the Italian Ministry of Education, University and Research (MIUR).

<sup>65</sup> <http://fermi.gsfc.nasa.gov/ssc/data/access/lat/BackgroundModels.html>

<sup>66</sup> For a detailed description of the GALPROP code the reader is referred to the dedicated website: <http://galprop.stanford.edu>

patches with spatially uniform spectral intensity to account for positive residuals. Some of these are in and about the GC, which makes interpretation of positive residuals after fitting additional templates and subtracting the IEM and point sources uncertain.

In this paper, an analysis is described of the  $\gamma$ -ray emission observed by the *Fermi*-LAT during the first 62 months of the mission toward the inner Milky Way that characterizes the  $15^\circ \times 15^\circ$  region in Galactic coordinates centered on the GC. This encompasses the innermost  $\sim 1$  kpc where the CR intensities, interstellar gas and radiation field densities are highest but most uncertain, and signatures of new physics may be detectable. The analysis uses multiple IEMs together with an iterative fitting procedure to determine the contributions by diffuse and discrete sources of high-energy  $\gamma$ -ray emission. The GALPROP CR propagation code is used to calculate components of IEMs that are fit to the *Fermi*-LAT data to predict the interstellar emission fore-/background toward the  $15^\circ \times 15^\circ$  region. Candidate locations of point sources are found using a wavelet-based algorithm (Damiani et al. 1997; Ciprini et al. 2007). These are used together with the IEMs to define a model for the emission of the region, which is then optimized in a maximum-likelihood fit to determine the contribution by CR-induced diffuse emission from the innermost  $\sim 1$  kpc and  $\gamma$ -ray point sources. This is the first self-consistent modeling balancing the various sources of  $\gamma$ -rays toward the inner Galaxy. The point sources found as a result are presented as the First *Fermi*-LAT Inner Galaxy point source catalog (1FIG), which is compared with the sources in the recent Third *Fermi*-LAT Source Catalog (3FGL; Acero et al. 2015b) for the same region.<sup>67</sup>

## 2. LARGE AREA TELESCOPE AND DATA SELECTION

The *Fermi* Gamma-ray Space Telescope was launched on 2008 June 11. The LAT, which is the main instrument on *Fermi*, is a pair-conversion telescope composed of a  $4 \times 4$  grid of towers, with each tower consisting of a silicon micro-strip tracker with interleaved tungsten foils for conversion of incident  $\gamma$ -rays into electron-positron pairs, mated with a hodoscopic cesium-iodide calorimeter. This grid of towers is covered by a segmented plastic scintillator anti-coincidence detector. The tracker is divided in two sections, “front” (4.1% radiation lengths [R.L.] per layer, first 12 layers below the anti-coincidence detector where a layer comprises the tungsten converter foil with two silicon detector planes and associated support structures) and “back” (19.3% R.L. per layer, next 4 layers) where the last two layers do not have conversion foils. The effective collecting areas of both sections are comparable, but the angular resolution for  $\gamma$ -rays that convert in the front section is approximately a factor of two better than for back-converting  $\gamma$ -rays. For the former the 68/95% containment radii of the point-spread function (PSF) are  $0^\circ.4/1^\circ.5$  at 1 GeV decreasing to  $0^\circ.1/0^\circ.3$  at 10 GeV. The LAT is sensitive to  $\gamma$ -rays with energies in the range from 20 MeV to over 300 GeV, and its on-axis effective area is  $\sim 8000$  cm<sup>2</sup> for energies  $>1$  GeV. The LAT is described in detail in Atwood et al. (2009), with specifics related to its on-orbit performance reported in Abdo et al. (2009b) and Ackermann et al. (2012b).

<sup>67</sup> The optimized IEMs, 1FIG, and sub-threshold source candidate lists are available at: [https://www-glast.stanford.edu/pub\\_data](https://www-glast.stanford.edu/pub_data).

The analysis described in this paper employs events with reconstructed energy in the range 1–100 GeV, where the effective area of the LAT is largest and not strongly dependent on energy. To allow the best separation between point sources and the structured interstellar emission in the analysis procedure (described below), only front-converting events are used.

Events and IRFs for the standard low-residual CR background “Clean” events from the Pass 7 event selections (Ackermann et al. 2012b)<sup>68</sup> are used. To minimize the contribution from the very bright Earth limb, the event selection and exposure calculation is restricted to zenith angles less than  $100^\circ$ .

Events are selected from approximately 62 months of data from 2008 August 11 until 2013 October 15. Exposure maps and the PSF for the pointing history of the observations were generated using the standard *Fermi*-LAT ScienceTools package (version 09-34-02) available from the FSSC.<sup>69</sup> For the  $15^\circ \times 15^\circ$  region about the direction toward the GC the resulting exposure is  $7 \times 10^{10}$  cm<sup>2</sup> s at 1 GeV.

## 3. METHODOLOGY

### 3.1. Interstellar Emission Models

The diffuse  $\gamma$ -ray emission is produced by the interaction of high-energy CRs with the interstellar gas and radiation fields. The limited angular resolution and statistics that are a characteristic of high-energy  $\gamma$ -ray data, coupled with the relatively intense interstellar emission at low latitudes, make accurate modeling of the latter important for characterizing all but the brightest point sources there (Abdo et al. 2010a; Nolan et al. 2012).

Two analysis approaches for studying the interstellar emission have been used by the *Fermi*-LAT Collaboration in previous works. Templates tracing  $\gamma$ -ray emission processes were used to determine the  $\gamma$ -ray emissivity of the interstellar gas within several kpc of the Sun (e.g., Abdo et al. 2009a, 2010c; Ackermann et al. 2011). The GALPROP code was used in an extensive study of IEMs constrained by local CR data and their correspondence with the *Fermi*-LAT data (Ackermann et al. 2012a). There are merits to both approaches. Fitting templates allows for fairly robust extraction of physical quantities, but is a method that is constrained by the assumption that interstellar medium (ISM) densities and other properties (gas-to-dust ratio,  $X_{\text{CO}}$ -factor, etc.) and CR spectra remain constant throughout the template, and that a suitable template is available (e.g., the inverse Compton [IC] component of the interstellar emission must be obtained using modeling codes)—see Strong et al. (1988) and Strong & Mattox (1996), and references therein. The GALPROP code can be used to predict the diffuse  $\gamma$ -ray emission throughout the Galaxy, and is capable of reproducing the observations at the  $\sim 20\%$  level. But the predictions of the propagation model based approach are limited by the quality of the inputs to the model calculations, which include the spatial distribution of CR sources and their injection spectra, and the spatial distribution of the interstellar gas density and the interstellar radiation field (ISRF) energy density. In this paper a combination of these methods is used where

<sup>68</sup> The reprocessed data and instrument response functions (IRFs) P7REP\_CLEAN\_V15 are employed. See [http://fermi.gsfc.nasa.gov/ssc/data/analysis/documentation/Pass7\\_usage.html](http://fermi.gsfc.nasa.gov/ssc/data/analysis/documentation/Pass7_usage.html)

<sup>69</sup> <http://fermi.gsfc.nasa.gov/ssc/data/analysis/>

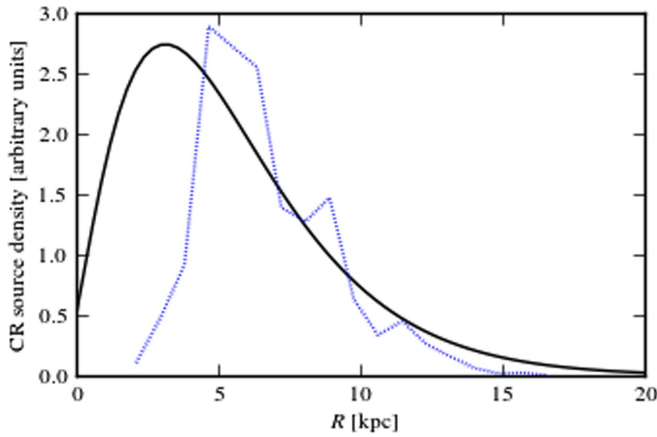


**Figure 1.** Galactocentric radial dependence of the spatial distribution of CR sources per unit volume. Line styles/colors: solid/black, Pulsars; dotted/blue, OB-stars.

the GALPROP code is employed to predict templates for the interstellar emission that are fit to the  $\gamma$ -ray data to estimate the foreground and background emission toward the inner Galaxy.

The results of the study by Ackermann et al. (2012a) are used for the baseline IEMs, which are further fit to the *Fermi*-LAT data. As a reminder, the Ackermann et al. (2012a) study used a grid of IEMs based on diffusion-reacceleration CR propagation models. The spatial distribution of CR sources, the H I spin temperature, H I column density corrections from dust emission, and the size of the CR confinement volume were the fixed parameters in the grid. For each grid point the diffusion coefficient was obtained by adjusting it to reproduce the observed CR secondary/primary ratios iterating with a fit to the  $\gamma$ -ray data for the  $X_{\text{CO}}$  distribution for each CR source model. The  $\gamma$ -ray emission for each of the IEMs in the grid was then compared with the *Fermi*-LAT data in the 200 MeV to 100 GeV energy range. The models in the Ackermann et al. (2012a) study agree at the  $\sim 10\%$ – $20\%$  level with the LAT observations over the sky.

A major uncertainty affecting predictions of the interstellar emission toward the inner Galaxy is the spatial distribution of CR sources. The Yusifov & Küçük (2004) pulsar distribution (“Pulsars”) and the distribution of OB-stars (“OBstars”; Bronfman et al. 2000) encapsulate this because they represent reasonable extremes for the Galactocentric radial dependence. Figure 1 shows the Galactocentric radial distributions of these CR source models. The Pulsars distribution is non-zero at the GC while the OBstars distribution goes to zero near  $\sim 2$  kpc. The models<sup>70</sup> assume an axisymmetric cylindrical geometry for the CR confinement volume with a halo height  $z_h = 6$  kpc and maximum radial boundary  $R_h = 30$  kpc. This halo height is the closest in the IEM grid<sup>71</sup> to the halo height distribution mean ( $\sim 5.5$  kpc) determined by Trotta et al. (2011); the exact value of the halo height is not critical for the analysis.

For the IEM fitting procedure the GALPROP code is used to calculate all-sky  $\gamma$ -ray intensity maps from 1 to 100 GeV for 10 logarithmically spaced energy bins per decade for the Pulsars and OBstars baseline models, which are normalized to local CR data, using the configuration files for each available from the

<sup>70</sup> Specifically, the  $^{\text{S}}\text{Y}^{\text{Z}}\text{6}^{\text{R}}\text{30}^{\text{T}}\text{150}^{\text{C}}\text{2}$  (Pulsars) and  $^{\text{S}}\text{O}^{\text{Z}}\text{6}^{\text{R}}\text{30}^{\text{T}}\text{150}^{\text{C}}\text{2}$  (OBstars) models from Ackermann et al. (2012a).

<sup>71</sup> Halo heights of 4, 6, 8, and 10 kpc were used in the Ackermann et al. (2012a) study.

**Table 1**  
Galactocentric Annular Boundaries

Annulus #	$R_{\text{min}}$ (kpc)	$R_{\text{max}}$ (kpc)	Longitude Range (Full)	Longitude Range (Tangent)
1	0	1.5	$-10^\circ \leq l \leq 10^\circ$	...
2	1.5	2.5	$-17^\circ \leq l \leq 17^\circ$	$10^\circ \leq  l  \leq 17^\circ$
3	2.5	3.5	$-24^\circ \leq l \leq 24^\circ$	$17^\circ \leq  l  \leq 24^\circ$
4	3.5	8.0	$-70^\circ \leq l \leq 70^\circ$	$24^\circ \leq  l  \leq 70^\circ$
5	8.0	10.0	$-180 \leq l \leq 180^\circ$	...
6	10.0	50.0	$-180 \leq l \leq 180^\circ$	...

GALPROP website.<sup>72</sup> The GALPROP code produces intensity maps in annuli that correspond to ranges in Galactocentric radii; the total intensity map for a given  $\gamma$ -ray production process ( $\pi^0$ -decay, IC, Bremsstrahlung) is the sum of all the annular intensity maps for that process, and the total predicted  $\gamma$ -ray sky from a GALPROP run is the sum of intensities from all processes. Table 1 lists the Galactocentric annuli and the corresponding longitude ranges for the full extent of each annulus, as well as the “tangent” regions that are used in the fitting procedure for the components interior to the solar circle (see Appendix B of Ackermann et al. 2012a, for a description of the generation of the H I and CO gas annuli).

The annular intensity maps are used as templates together with an isotropic component and a model for  $\gamma$ -ray emission associated with Loop I employing a two-component spatial template from Wolleben (2007) with a power-law spectral model for each, and point sources from the 3FGL source catalog.<sup>73</sup> This combined model is fit to the *Fermi*-LAT data excluding the  $15^\circ \times 15^\circ$  region about the GC using a maximum-likelihood method<sup>74</sup>, but with the point-source normalizations and spectral shapes held constant. Because they make only a small contribution this does not significantly affect the determination of the IEM parameters.

Two IEMs for each of the Pulsars and OBstars models—4 in total—are constructed. The two variants for each model are termed “intensity-scaled” and “index-scaled.” The normalization parameters for the templates are determined in a series of fits to the data, starting at high latitudes for the local components and then working from the outer Galaxy to the inner Galaxy, always fixing the already determined normalization parameters in subsequent fits. For the intensity-scaled variants only the normalizations of the individual intensity maps are allowed to change. For the index-scaled variants the same fitting procedure is followed, but additional degrees of freedom are allowed to the spectrum of the gas-related interstellar emission when fitting to the annuli interior to the solar circle. The details of the procedure for the intensity-scaled variants are given in Appendix A. The motivation for the index-scaled variants is described further below.

Figure 2 upper and center panels show the fractional residuals,  $(\text{data} - \text{model})/\text{model}$ , for 1–10 GeV energies<sup>75</sup>

<sup>72</sup> <http://galprop.stanford.edu/PaperIISuppMaterial/>

<sup>73</sup> This allows for discrimination between structured interstellar emission and point sources close to the Galactic plane when developing the fore-/background IEMs.

<sup>74</sup> The GaRDian code is used, which forward folds the model with the instrument response and PSF for the likelihood evaluation—see Appendix A of Ackermann et al. (2012a).

<sup>75</sup> The  $>10$  GeV residuals show similar characteristics to the 3.16–10 GeV energy band, but they are not shown here because of their relatively limited statistics.

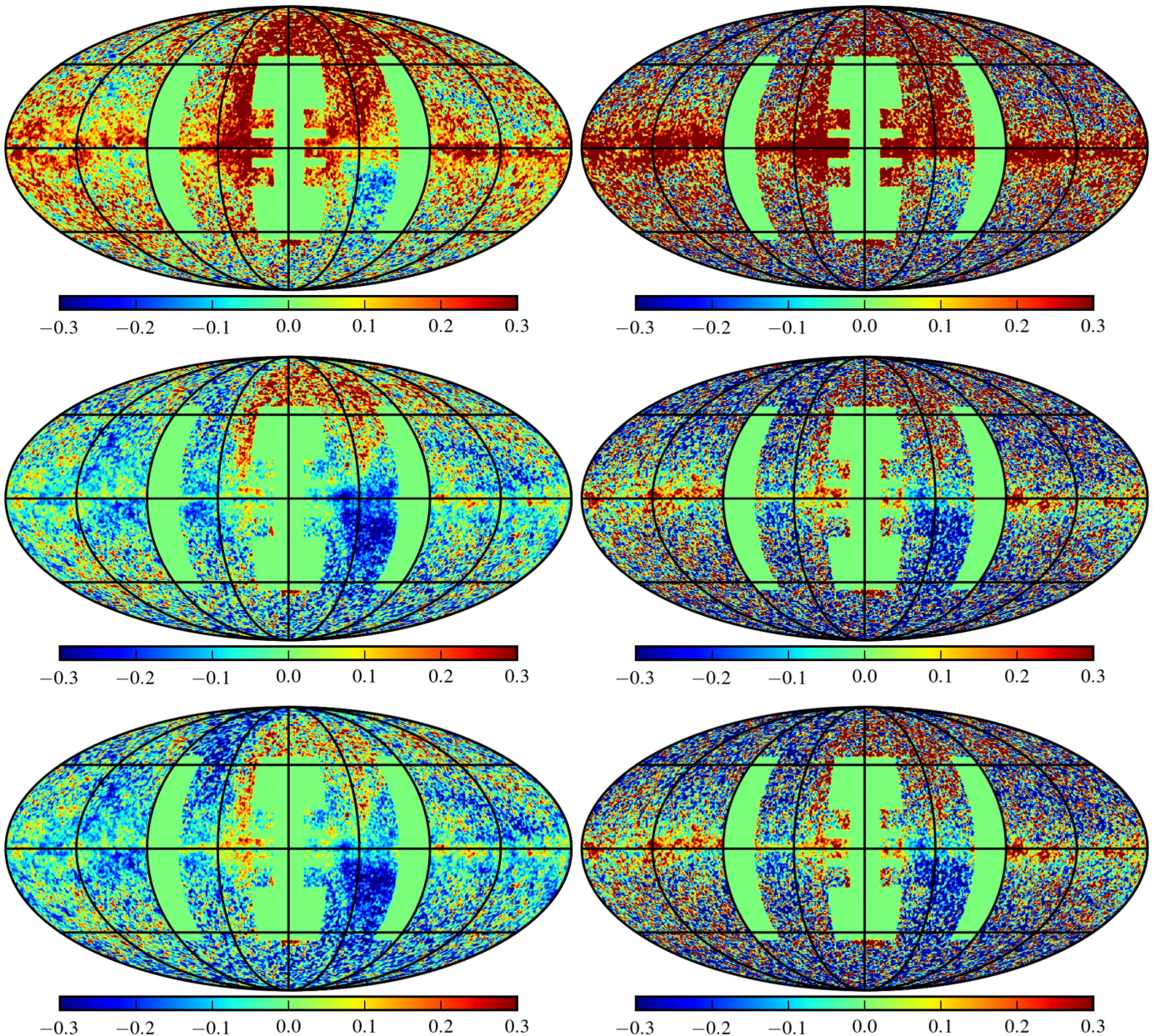


**Figure 2.** Residual fractional counts  $(data - model)/model$  in the 1–3.16 GeV (left) and 3.16–10 GeV (right) energy ranges for the baseline Pulsars model (upper), the intensity-scaled Pulsars model (center), and the index-scaled Pulsars model (lower) fitted following the procedure described in the text. The isotropic component determined from the high-latitude fit is included in the baseline model (upper panels) for the fractional residual calculation. The baseline model does not include a model for the Loop-I SNR, resulting in the large positive residuals in the northern Galactic hemisphere. The maps are calculated for a HEALPix order 8 pixelization ( $\sim 0.23^\circ$  resolution) and smoothed with a  $1^\circ$  FWHM Gaussian. Regions not used for the IEM tuning procedure are masked. The positive residual at mid-to-high latitudes interior to the solar circle is due to mismatch between the data and the relatively simple Loop I model. The residuals close to the plane from this mismatch are lower and do not affect the analysis of the  $15^\circ \times 15^\circ$  region about the GC.

for the baseline and intensity-scaled Pulsars model. The isotropic component determined for the intensity-scaled IEM has been included in the baseline model for the fractional calculation to show the relative differences from the Galactic components of the IEMs. The regions not used in the fitting procedure are explicitly masked in the figure. They are not used because of localized extended excesses that are most likely unrelated to the large-scale interstellar emission. In particular, the band covering  $70^\circ \leq l \leq 90^\circ$  includes the Cygnus region ( $l \sim 75^\circ - 85^\circ$ ) around the Galactic plane; the corresponding band for negative longitudes is a consequence of the axisymmetric nature of the model being used. The range

$90^\circ \leq l \leq 270^\circ$  is used to constrain the IC emission from annulus 5 so the data out of the plane from the  $70^\circ \leq l \leq 90^\circ$  region is not required to constrain this component. The  $-20^\circ \leq l \leq 20^\circ$ ,  $10^\circ \leq |b| \leq 50^\circ$  region where the *Fermi* haze/bubbles have been detected is also excluded. Including these regions in the fitting procedure would bias the normalization of the IEM components because models for these features are not included in this study.

Outside of the Galactic plane the fractional residuals are substantially reduced for the intensity-scaled IEM compared to the baseline. This is due to the scaling of the  $\pi^0$ -decay interstellar emission for the local annulus, and of the IC

component generally. The coefficient for the local gas (annulus 5) interstellar emission is adjusted upward (see Table 5 in Appendix A for a full list of IEM coefficients). Meanwhile, the coefficients of the IC intensity for the local and other annuli interior to the solar circle are increased compared to the baseline IEM. Ackermann et al. (2012a) also found that better fits to the  $\gamma$ -ray data were generally obtained by increasing the IC intensity for large regions of the sky for the baseline IEMs. While the GALPROP version used by Ackermann et al. (2012a) only allowed the calculation of all-sky IC intensity maps, the decomposition of the IC intensity into Galactocentric annuli used here enables mismodeling of the IC emission due to uncertainties of the gradients in the CR electron and ISRF distributions to be more accurately treated (Section 4.1).

Along the Galactic plane the  $\gtrsim 30\%$  under-prediction by the baseline model is reduced to  $\lesssim \pm 10\%$  after this scaling, except for scattered regions. The longitude range  $l \sim -(15-70)^\circ$  is the largest such region where the intensity-scaled IEM over-predicts the data by  $\sim 20\%-30\%$  in the 1–3.16 GeV band. Within  $\sim 10^\circ$  of the mid-plane this may indicate that the spectrum of the IEM related to the CR nuclei/gas interaction ( $\pi^0$ -decay) in this region is too soft. To account for this, additional degrees of freedom to the spectrum<sup>76</sup> of the  $\pi^0$ -decay interstellar emission are allowed, and the model is refitted for annuli interior to the solar circle following the same sequence of regions as for the intensity-scaled IEMs—this is the “index-scaled” IEM variant.

Figure 2 lower panels show the fractional residuals for the index-scaled variants of the Pulsars IEM. The fractional difference for the  $l \sim -(15-70)^\circ$  region in the 1–3.16 GeV energy range is reduced to  $\lesssim \pm 10\%$  with a slight increase in the residual for the corresponding positive longitude range. At mid-to-high latitudes the residual is reduced because the IC for the annuli interior to the solar circle and Loop-I model are also refit.

The intensity-scaled IEM gives a lower residual for positive longitudes inside the solar circle around 1 GeV, while the index-scaled variant is closer to the data at negative longitudes. The converse appears at higher energies where instead the intensity-scaled IEM gives lower residuals at negative longitudes than the index-scaled variant. The underlying axisymmetric geometry for the IEMs is partly responsible for this: there is not enough freedom in the model parameters, even for the index-scaled variant, to account for differences due to any error in the assumption of an average CR distribution for each Galactocentric annulus (the limitations of the IEM tuning procedure and resulting models are discussed further in Section 5.4). Qualitatively, similar results for the scaled OBstars IEMs (not shown) are obtained.

It is not straightforward to identify a best IEM after fitting because the qualitative improvement for each over the corresponding baseline IEM is similar. Consequently, all 4 (Pulsars/OBstars, intensity-/index-scaled) IEMs are used to estimate the fore-/background toward the  $15^\circ \times 15^\circ$  region about the GC below.

### 3.2. Modeling $15^\circ \times 15^\circ$ Region about the GC

#### 3.2.1. Point-source Candidates

Point-source candidates (“seeds”) are identified using the wavelet analysis algorithm *PGWave* (Damiani et al. 1997; Ciprini et al. 2007), one of the source detection algorithms employed in the development of the *Fermi*-LAT catalogs. The method finds seeds subject to a user-specified signal-to-noise criterion ( $3\sigma$  is used) based on the assumption of a locally constant background. This step identifies true point sources, as well as structures in the interstellar emission that are indistinguishable from point sources due to the finite angular resolution and statistics of the *Fermi*-LAT data, without dependence on the specifics of an IEM.

Four energy intervals with spacing  $\Delta \log_{10} E = 0.5$  covering 1–100 GeV, i.e., 1–3.16, 3.16–10, 10–31.6, and 31.6–100 GeV are used. *PGWave* is run for each energy interval and seeds that are above the signal/noise threshold are retained. The seeds found for each energy interval are combined. Seed locations within the 68% containment radius of the PSF for the highest energy interval ( $\sim 0.1$ ) are considered duplicate. Duplicate seeds are combined at the location determined from the highest energy interval that exceeds the signal-to-noise criterion. Over the energy bands there are 142 unique seeds.

*PGWave* does not provide spectral information for the point-source seeds. The spectra of the candidates are initially evaluated using *PointLike*, a package for maximum-likelihood analysis of *Fermi*-LAT data (Kerr 2010; Lande et al. 2012). *PointLike* also has the capability of optimising positions for seeds from the *PGWave*-determined list, but it requires an IEM. The Pulsar and OBstars intensity-scaled IEMs are used for this step. The point-source parameters are allowed to vary for the *PointLike* optimization, while the IEM and isotropic components of the background model are held constant. This enables the optimization of the positions for the point-source candidates as well as determine preliminary spectral parameters.

A PowerLaw (PL)<sup>77</sup> is assigned as the spectral model to each seed and the spectral parameters are fit to make initial evaluations for the fluxes, spectral indices, and a test statistic (*TS*; Mattox et al. 1996). Because no spectral information for the seeds are initially available the parameters for each are fit with all other candidates set to zero and held constant. Using the trial spectra, the seeds are refit 10 at a time ordered by decreasing *PointLike*-determined *TS*, with the flux normalization of the other candidates held constant. The combined list of candidates is refit using the information from the subsets to obtain a set of stable power-law spectral parameters.

Following the pass to determine initial PL spectral models, the individual candidates ranked by the *PointLike*-determined *TS* in descending order are refit with two hypotheses for the spectral properties, PL and LogParabola (LP).<sup>78,79</sup> The following criteria are used to choose between the spectral models: if the *PointLike*-determined *TS* is  $< 50$ , a PL spectrum is assigned to the point-source seed. If the *PointLike*-determined *TS* is  $> 50$ , the seed is fit with a PL and a LP

<sup>77</sup> PL:  $dN/dE = N_0 E^{-\alpha}$  with parameters  $N_0$  and  $\alpha$ .

<sup>78</sup> LP:  $dN/dE = N_0 (E/E_b)^{-\alpha-\beta \log(E/E_b)}$  with parameter tuple  $N_0$ ,  $\alpha$ ,  $\beta$ , and  $E_b$ .

<sup>79</sup> An exponential cut-off power law was not included in the spectral templates, as employed in the 3FGL, because of the limited energy range for the current study.

<sup>76</sup> See Appendix A.

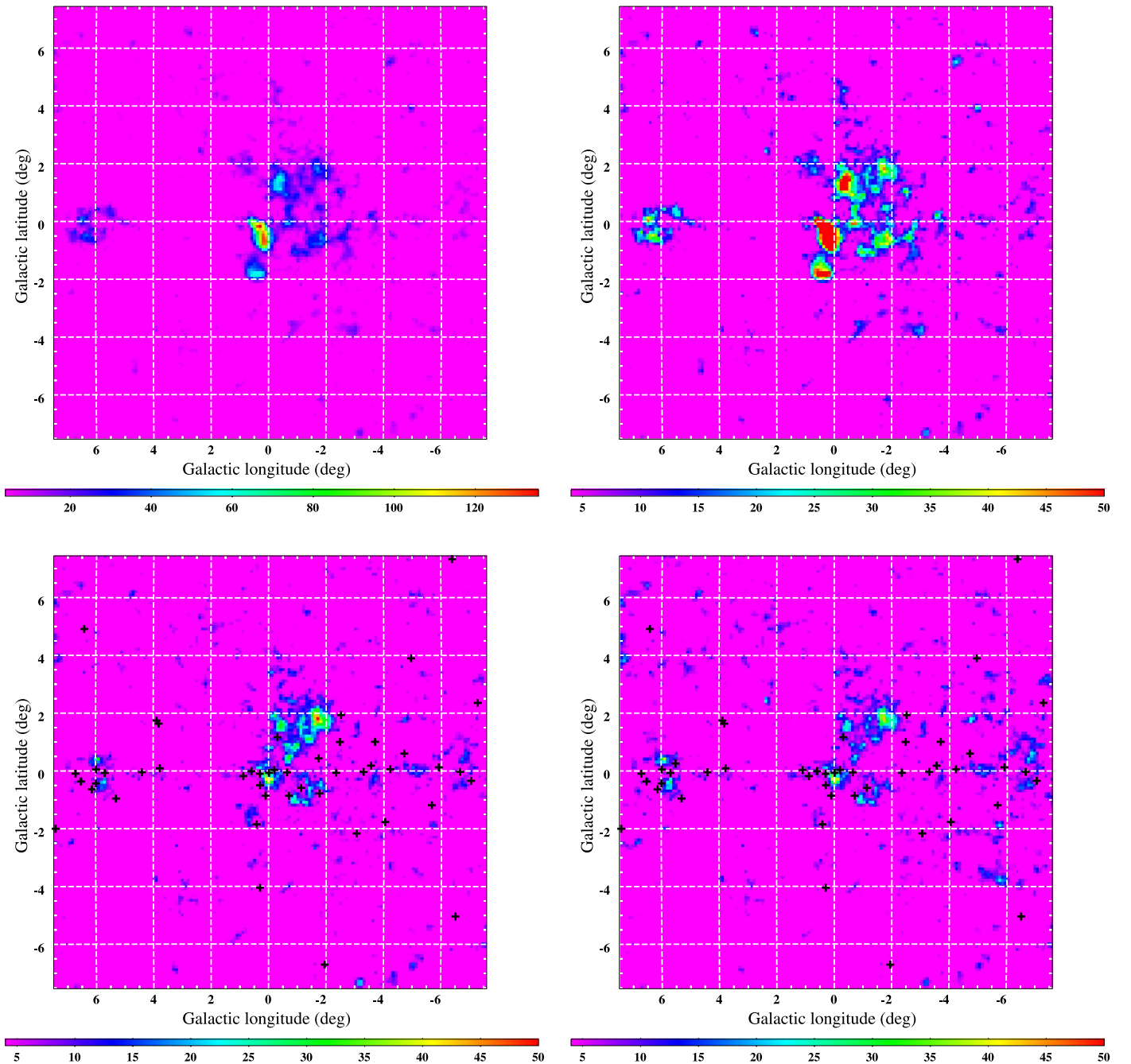


**Figure 3.** *TS* map corresponding to the maximum-likelihood result including the Pulsars intensity-scaled IEM after the first iteration for the  $15^\circ \times 15^\circ$  region about the GC (top panels; left: full scale, right:  $TS < 50$ ) and after the second iteration (bottom, left panel). The *TS* map for the only iteration of the analysis for the OBstars intensity-scaled model is also shown (bottom, right panel). The black crosses indicate the location of the  $TS > 25$  point sources.

spectrum, allowing also the spectral parameters for other candidates within  $3^\circ$  to vary. If  $TS(LP) > TS(PL) + 9$ , a LP spectrum is assigned to the seed; a PL spectrum is assigned if this condition is not met.

The spectra of the combined list of candidates are refit and only candidates with *PointLike*-determined  $TS > 9$  retained for the maximum-likelihood fit (Section 3.2.2). The optimization step reduces the number of candidates by  $\approx 60\%$  from the initial *PGWave*-identified list.

For the only extended source that has been previously identified in the region, the W28 supernova remnant (Abdo et al. 2010b), the spatial template and spectral model employed

for the 3FGL analysis were used. The spectral parameters are refit during the maximum-likelihood procedure.

### 3.2.2. Combined Interstellar Emission and Point Source Fit

Point-source candidates are combined with their *PointLike* trial spectra together with the IEMs described in Section 3.1 in a second maximum-likelihood fit. A binned likelihood fit is performed using the *Fermi* ScienceTool *glike*. The templates for the  $\pi^0$ -decay related  $\gamma$ -ray intensity from H I and CO, and the IC emission, in annulus 1 are freely scaled in the fitting procedure. The size of these templates is slightly larger than the

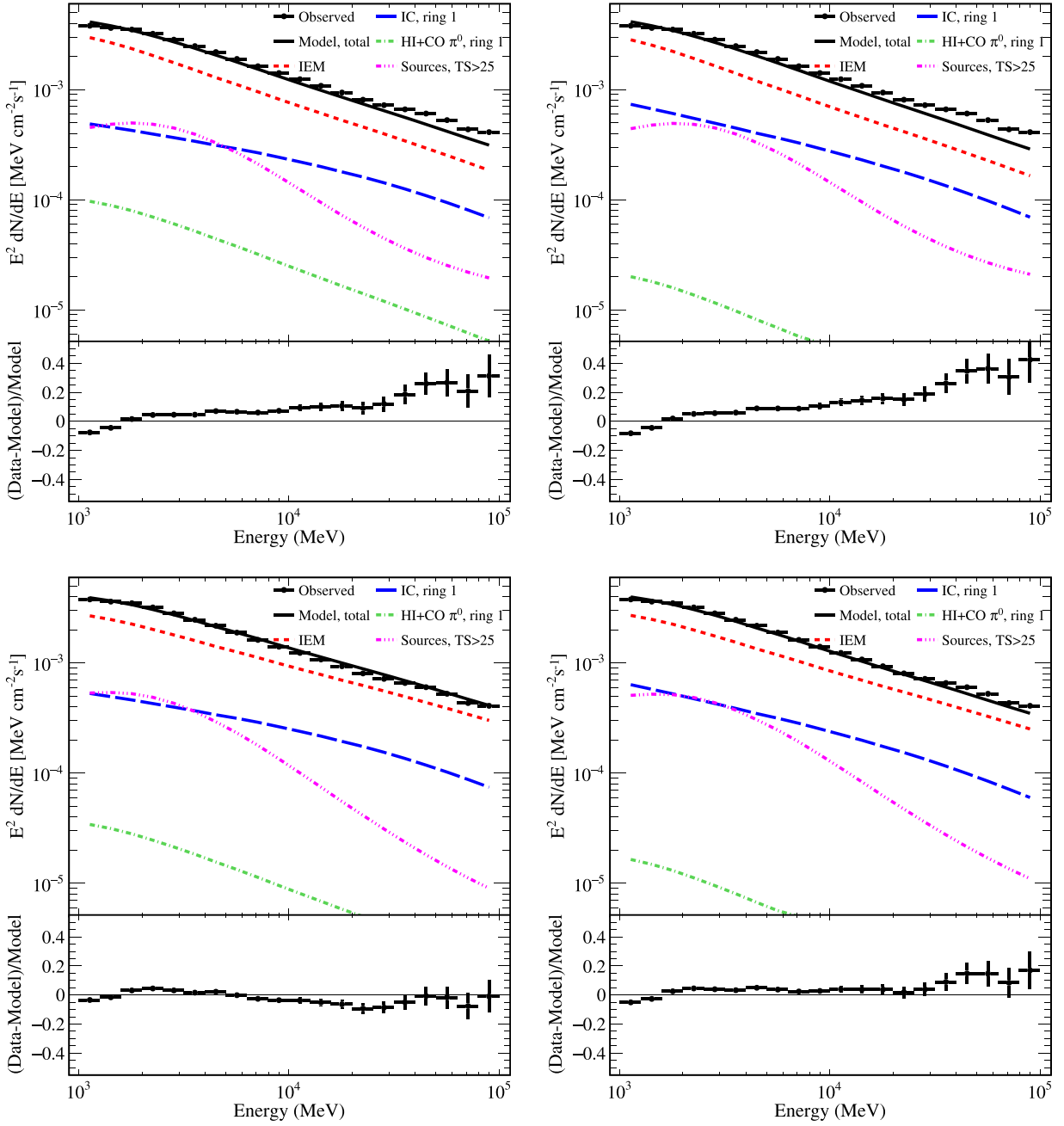


**Figure 4.** Differential fluxes for the  $15^\circ \times 15^\circ$  region about the GC for the four IEMs constrained as described in Section 3.1. Upper row shows the results for the intensity-scaled IEMs based on the Pulsars (left) and OBStars (right) source distributions. Lower row shows the results for the index-scaled IEMs based on the Pulsars (left) and OBStars (right) source distributions. Line styles: solid (total model), long-dash (IC, annulus 1), dot-dash (H I and CO gas  $\pi^0$ -decay, annulus 1), dot-dot-dot-dash (point sources), dash (Galactic interstellar emission excluding annulus 1 for IC, H I and CO gas  $\pi^0$ -decay). Solid circles: data.

$15^\circ \times 15^\circ$  region so the fit results are only strictly valid within  $\sim 1$  kpc of the GC rather than the formal 1.5 kpc extent of annulus 1. The annulus 1 templates are fixed in spatial distribution and spectra to the respective GALPROP predictions; for the index-scaled IEM variants allowing additional spectral freedom to the annulus 1  $\pi^0$ -decay components was tried as well, but the fits were unstable. The contributions of the IEM and the isotropic component, as determined by the procedure outlined in Section 3.1, are held constant in the fit. The scaling factors for the interstellar emission templates for annulus 1 are fit concurrently with the spectral parameters of the point-source seeds. Because of the large number of point-source seeds, the fit is performed iteratively, starting from the

largest  $TS$  candidates and progressively fitting the lower  $TS$  ones while the rest are fixed to their best fit values from the previous iteration. The normalization of the aforementioned innermost ring IEM intensities are free parameters in each iteration.

The results of the maximum-likelihood fit are values and confidence ranges for the coefficients of the H I annulus 1, CO annulus 1, IC annulus 1, as well as the  $TS$ , fluxes and spectra for the point sources. All point sources with a maximum-likelihood determined  $TS > 9$  are included in the model; a  $TS = 25$  threshold is used for a formal detection, corresponding to just over  $4\sigma$  as for the 3FGL and other *Fermi*-LAT source catalogs.

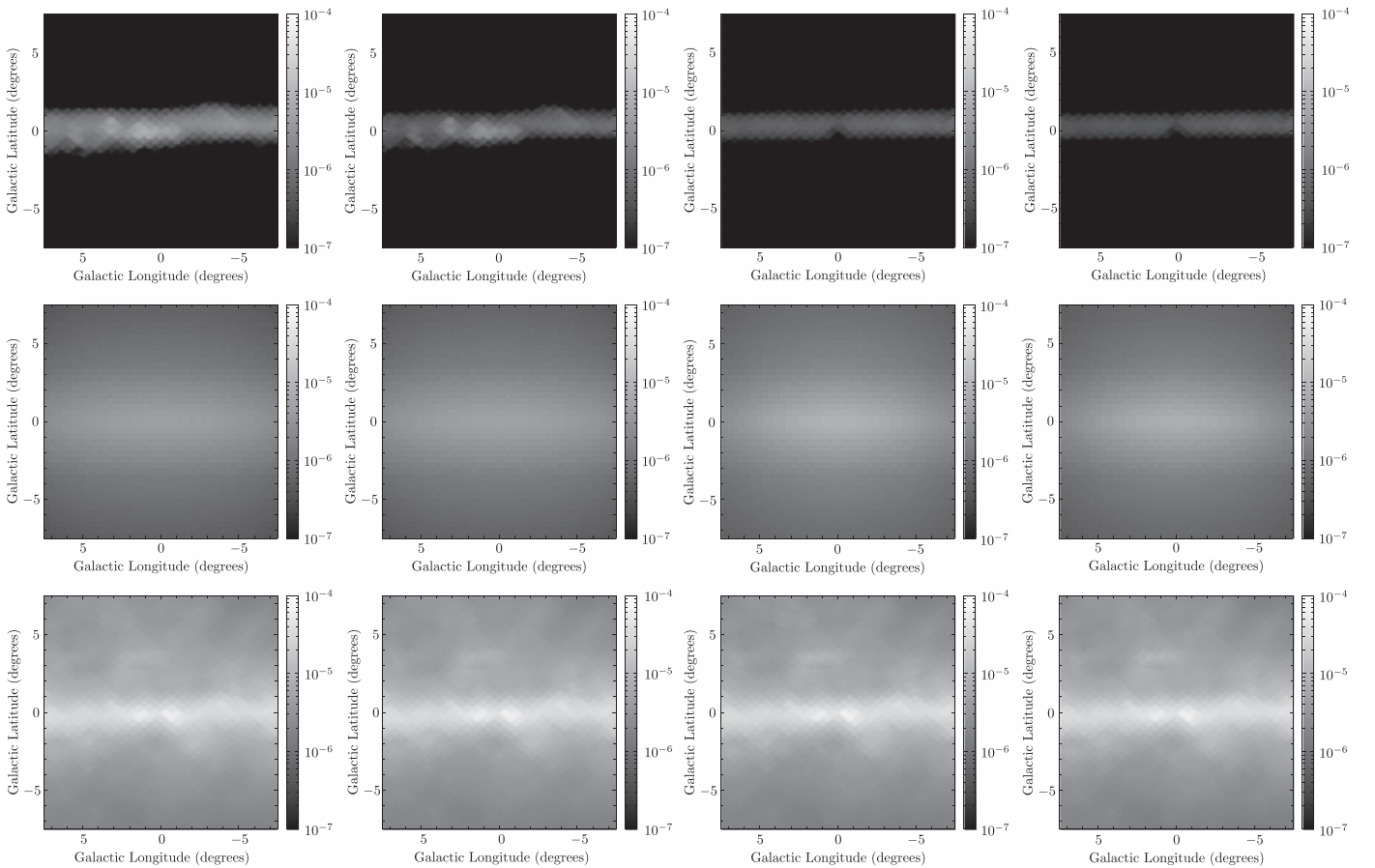


**Figure 5.** Interstellar emission model components  $>1$  GeV for the fit results for the  $15^\circ \times 15^\circ$  region about the GC and the fore-/background. First column: Pulsars intensity-scaled; second column: Pulsars, index-scaled; third column: OBstars, intensity-scaled; fourth column: OBstars, index-scaled. First row:  $\pi^0$ -decay intensity for annulus 1 after the maximum-likelihood fit (Section 3.2.2); second row: IC intensity for annulus 1 after fitting; third row: total fore-/background interstellar emission. Color scale units:  $\text{cm}^{-2} \text{s}^{-1} \text{sr}^{-1}$ .

### 3.2.3. Residual Maps and Iteration

A potential drawback of using the wavelet detection algorithm is that fainter point sources may be missed with a single iteration. This is remedied in this analysis by iterating the point-source seed detection on the residual maps following the maximum-likelihood fit and rerunning the analysis chain. The iteration is made until there are no new significant excesses in the  $TS$  map of the region that satisfy the signal-to-noise criterion adopted in the *PGWave* detection step. The  $TS$  map is determined by moving a putative point source with a PL with spectral index  $-2$  using *PointLike* through a grid of locations in the region and by maximising the likelihood function at each location. The positions of peaks with  $TS > 9$  are added to the source model.

Figure 3 (left panel) shows the  $TS$  map following the *glike* maximum-likelihood fit using these candidates in the first full iteration for the Pulsars intensity-scaled IEM. Some significant excesses remain after the initial pass, in particular around the GC. The *PGWave* and *PointLike* seed-finding and optimization steps are repeated (Section 3.2.1), finding 37 additional candidates with a *PointLike*-assigned  $TS > 9$  for the Pulsars intensity-scaled IEM. The left bottom panel in Figure 3 shows the  $TS$  map after the second full iteration of the analysis of the  $15^\circ \times 15^\circ$  region for this IEM. Some excesses with  $TS > 25$  remain. However, these correspond to point-source candidates reported by *PGWave* in the first iteration that were rejected

because their *glike*-assigned  $TS < 9$ , possibly due to structures having angular extensions that are larger than the PSF core.

The procedure for the initial optimization, binned likelihood fit, and iteration is also done using the OBstars intensity-scaled IEM. This yields 85 point source candidates with *PointLike*-assigned  $TS > 9$ . The point-source candidates are combined with their *PointLike* trial spectra together with the OBstars intensity-scaled IEM in a maximum-likelihood fit using *glike*, following the same procedure as outlined above. The  $TS$  map after the *glike* maximum-likelihood fit for this model is shown in the bottom right panel of Figure 3. The results are very similar to the second iteration of the analysis using the Pulsars intensity-scaled model. Consequently, no further iteration is made for the OBstars model.

For the Pulsars and OBstars index-scaled variants, the point-source seeds with  $TS > 9$  from the corresponding intensity-scaled IEM are used in the source model for the maximum-likelihood fit. This procedure yields  $TS$  maps that are very similar to the respective intensity-scaled counterparts. The results are summarized in Section 4.

## 4. RESULTS

### 4.1. Interstellar Emission

Figure 4 shows the differential spectra of the individual components obtained for the 4 IEMs integrated over the

**Table 2**  
Fluxes of the Components<sup>a</sup> for  $15^\circ \times 15^\circ$  region about GC

Interstellar Emission Model	Energy Band (GeV)	Annulus 1		Point Sources		Fore-/background		Isotropic	Model	Data
		$\pi^0$ -decay	IC	$\pi^0$ -decay	IC	IC	Brem	Total		
<b>Pulsars</b>										
Intensity-scaled	1.00–3.16	$6.1 \pm 1.1$	$32.5 \pm 0.6$	$36.3 \pm 1.2$	135	23	24	2.3	$259 \pm 3$	$251 \pm 13^b$
	3.16–10.00	$1.0 \pm 0.2$	$7.1 \pm 0.1$	$7.3 \pm 0.2$	21	5.4	1.7	0.6	$44.1 \pm 0.5$	$44 \pm 3$
	10.00–31.62	$0.13 \pm 0.02$	$1.41 \pm 0.03$	$0.81 \pm 0.04$	2.9	1.2	0.14	0.17	$6.7 \pm 0.1$	$6.8 \pm 0.7$
	31.62–100.00	$0.02^c$	$0.24^c$	$0.11 \pm 0.01$	0.4	0.2	0.01	0.04	$1.04 \pm 0.02$	$1.2 \pm 0.2$
<b>Pulsars</b>										
Index-scaled	1.00–3.16	$2.1 \pm 1.1$	$35.5 \pm 0.6$	$37.9 \pm 1.5$	127	25	...	...	$254 \pm 3$	...
	3.16–10.00	$0.3 \pm 0.2$	$7.8 \pm 0.1$	$6.6 \pm 0.2$	25	6	...	...	$48 \pm 0.5$	...
	10.00–31.62	$0.05 \pm 0.02$	$1.54 \pm 0.03$	$0.62 \pm 0.03$	4.2	1.3	...	...	$8.0 \pm 0.1$	...
	31.62–100.00	$0.01^c$	$0.3^c$	$0.07 \pm 0.01$	0.75	0.23	...	...	$1.37 \pm 0.01$	...
<b>OBstars</b>										
Intensity-scaled	1.00–3.16	$1.3 \pm 0.5$	$47.0 \pm 0.6$	$35.7 \pm 1.2$	128	23	21	2.6	$259 \pm 2$	...
	3.16–10.00	$0.2 \pm 0.1$	$9.1 \pm 0.1$	$7.3 \pm 0.2$	19	5.1	1.4	0.7	$43.3 \pm 0.4$	...
	10.00–31.62	$0.02 \pm 0.01$	$1.62 \pm 0.02$	$0.8 \pm 0.1$	2.6	1.1	0.12	0.16	$6.4 \pm 0.1$	...
	31.62–100.00	$--^c$	$0.25^c$	$0.11 \pm 0.01$	0.4	0.2	0.01	0.03	$0.97 \pm 0.02$	...
<b>OBstars</b>										
Index-scaled	1.00–3.16	$1.0 \pm 0.5$	$40.9 \pm 0.6$	$38.3 \pm 1.3$	135	19	...	...	$257 \pm 2$	...
	3.16–10.00	$0.14 \pm 0.07$	$7.9 \pm 0.1$	$6.8 \pm 0.2$	24	4.3	...	...	$45.6 \pm 0.4$	...
	10.00–31.62	$0.02 \pm 0.01$	$1.41 \pm 0.02$	$0.69 \pm 0.04$	3.9	0.9	...	...	$7.2 \pm 0.1$	...
	31.62–100.00	$--^c$	$0.22^c$	$0.08 \pm 0.01$	0.6	0.2	...	...	$1.15 \pm 0.01$	...

**Notes.**<sup>a</sup> Units:  $10^{-8}$  ph cm $^{-2}$  s $^{-1}$ .<sup>b</sup> The errors are dominated by systematic uncertainties from the effective area, see Ackermann et al. (2012b) for details.<sup>c</sup> Flux and/or statistical uncertainty below  $10^{-10}$  ph cm $^{-2}$  s $^{-1}$ .

$15^\circ \times 15^\circ$  region about the GC. The figure separates the emission components in terms of the contributions by  $\pi^0$ -decay and IC for annulus 1, the interstellar emission fore-/background, and point sources over the region. As expected, the fore-/background dominates for each IEM, which is predominantly  $\pi^0$ -decay in origin. IC scattering is the dominant interstellar emission component over the inner  $\sim 1$  kpc. This contrasts with the predictions of the baseline Pulsars and OBstars IEMs, in which the neutral gas  $\pi^0$ -decay interstellar emission components over the same region have similar fluxes. Combined, the GALPROP-predicted H I and CO-related  $\pi^0$ -decay annulus 1 templates are brighter by up to an order of magnitude than the IC emission for either model. The fit for the  $15^\circ \times 15^\circ$  region preferentially adjusts the annulus 1 IC component while suppressing the H I and CO-related  $\pi^0$ -decay templates for all IEMs. The scaling factors for the annulus 1 IC templates are  $\sim 6$ – $30$ , with higher values for the OBstars IEM variants. While the difference in the scaling factors between the IEMs is large, the final flux determined for the IC over annulus 1 over all four IEMs is within a factor  $\sim 1.5$ .

Figure 5 shows the spatial distribution of the individual components over the  $15^\circ \times 15^\circ$  region about the GC for energies  $> 1$  GeV for each IEM. As noted above, the fore-/background interstellar emission is clearly the brightest component. Although the intensity scale does not directly show a strong variation within  $\sim \pm 1^\circ$  of the mid-plane the fore-/background over the four IEMs varies by  $\sim 30\%$ , which is similar to elsewhere in the plane. Outside of the plane the brightness of individual features varies. For example, around  $l \sim 0^\circ$ – $2^\circ$ ,  $b \sim 3^\circ$  the Pulsars IEMs are dimmer.

Other low-intensity structures appear to change subtly for the different IEMs. This is predominantly due to scaling of the  $\pi^0$ -decay emission from annuli 2–4, which is discussed further below.

The IC intensity is more peaked toward the GC for the OBstars model compared to the Pulsars IEM. This is due to spatial distributions of CR sources employed for the respective IEMs, which result in different spatial distributions for the propagated CR electron intensities over the inner few kpcs. The paucity of sources within a few kpc of the GC for the OBstars IEM gives a constant intensity because the electrons must diffuse from larger Galactocentric radii. On the other hand, the Pulsars source distribution peaks around a few kpc and is non-zero in toward the GC, giving a higher electron intensity with a gradient. Combined with the spatial distribution over the same region of the ISRF intensity, which peaks at the GC, the results are IC templates that are broader (Pulsars) or more peaked (OBstars) for annulus 1.

Table 2 gives the fluxes of the different components integrated over the four energy bins from 1 to 100 GeV. Trends that can explain the low level of emission associated with the annulus 1  $\pi^0$ -decay component are not readily apparent. Because the fore-/background is held constant for the maximum-likelihood fit over the  $15^\circ \times 15^\circ$  region (Section 3.2.2) there is no correlation matrix with the IEM that can be examined to determine degeneracies for the structured interstellar emission component.

But some understanding of the effect of the fore-/background can be inferred from examining the fluxes per annuli for each of the IEMs (see Table 6 in Appendix A). The IEM

**Table 3**  
Point Sources Detected with  $TS > 25$  for Pulsars Intensity-scaled IEM for the  $15^\circ \times 15^\circ$  Region about the GC

Name IFIG	$l$ (degrees)	$b$ (degrees)	$\Delta\theta$ (degrees)	$TS$	$F_{1-100 \text{ GeV}}^a$ ( $10^{-9} \text{ ph cm}^{-2} \text{ s}^{-1}$ )	Type <sup>b</sup>	Fermi Catalog Association
J1701.1–3004	353.60	7.34	0.03	165	2.61/2.62/2.54/2.65	LP	3FGL J1701.2–3006
J1717.5–3342	352.74	2.36	0.03	113	3.13/3.58/3.73/3.78	LP	3FGL J1717.8–3342
J1718.0–3056	355.05	3.90	0.04	26	0.74/0.93/0.92/0.90	PL	3FGL J1718.1–3056
J1728.6–3433	353.36	−0.03	0.04	42	3.65/4.38/3.70/3.85	PL	...
J1729.1–3502	352.98	−0.34	0.05	87	3.76/4.10/4.01/3.79	LP	...
J1730.2–3351	354.10	0.13	0.08	34	3.41/4.22/3.43/3.58	PL	...
J1731.3–3235	355.30	0.60	0.05	80	3.97/5.01/4.19/4.89	LP	...
J1731.6–3001	357.49	1.94	0.03	120	3.13/3.68/3.04/3.18	LP	3FGL J1731.8–3001
J1732.3–3131	356.31	1.01	0.01	3339	36.00/37.44/36.32/37.46	LP	3FGL J1732.5–3130
J1734.6–3228	355.78	0.06	0.07	30	2.01/2.53/1.72/1.54	PL	...
J1735.4–3030	357.52	1.00	0.05	40	2.82/3.40/2.54/2.95	PL	...
J1736.1–3150	356.45	0.18	0.09	35	1.74/1.64/1.53/1.40	PL	...
J1736.1–3422	354.34	−1.19	0.05	47	2.34/2.64/2.68/2.74	PL	...
J1737.4–3144	356.71	−0.03	0.06	67	3.52/3.82/2.80/2.88	LP	...
J1739.4–3010	358.27	0.44	0.09	39	3.61/4.64/2.44/3.17	PL	...
J1740.1–3057	357.66	−0.06	0.04	43	3.11/3.48/2.10/2.86	PL	...
J1740.2–2834	359.69	1.17	0.11	76	3.96/4.73/2.81/3.53	LP	3FGL J1740.5–2843
J1741.5–2538	2.37	2.44	0.04	25	0.53/0.61/0.51/0.00	PL	3FGL J1741.9–2539
J1741.5–2054	6.41	4.92	0.02	1679	15.16/15.72/15.60/15.67	LP	3FGL J1741.9–2054
J1742.5–3318	355.96	−1.77	0.07	104	3.42/3.92/3.51/3.73	LP	3FGL J1742.6–3321
J1744.2–2930	359.36	−0.05	0.05	106	7.51/9.06/6.68/7.86	LP	...
J1744.3–3051	358.23	−0.78	0.15	31	2.36/2.33/1.73/1.85	PL	3FGL J1744.7–3043
J1745.0–2905	359.80	0.03	0.04	270	16.14/15.98/14.52/17.38	LP	...
J1745.1–3012	358.87	−0.59	0.05	123	7.79/8.57/6.42/7.76	LP	3FGL J1745.1–3011
J1745.5–2859	359.98	−0.07	0.01	3063	56.82/57.61/56.57/56.99	LP	...
J1746.4–2843	0.30	−0.10	0.04	330	19.00/18.53/18.90/18.93	LP	...
J1746.5–3240	356.95	−2.16	0.03	358	7.53/8.15/7.51/7.94	LP	3FGL J1746.8–3240
J1747.0–2826	0.59	−0.01	0.04	169	11.24/13.11/11.01/12.45	LP	3FGL J1747.0–2828
J1747.2–2959	359.29	−0.86	0.02	879	20.38/20.61/19.30/21.12	LP	3FGL J1747.2–2958
J1747.6–2442	3.88	1.75	0.04	36	0.87/1.38/0.89/1.02	LP	...
J1748.1–2449	3.81	1.64	0.03	446	9.07/9.29/9.36/9.56	LP	3FGL J1748.0–2447
J1748.2–2856	0.29	−0.50	0.17	90	6.75/7.36/6.89/7.30	LP	3FGL J1747.7–2904
J1748.2–2816	0.88	−0.18	0.02	377	11.20/11.97/11.86/11.78	LP	3FGL J1748.3–2815c
J1749.1–2917	0.10	−0.86	0.12	92	4.97/5.30/4.21/4.43	LP	3FGL J1749.2–2911
J1750.2–3705	353.50	−5.04	0.06	49	1.41/1.45/1.45/1.55	PL	3FGL J1750.2–3704
J1753.5–2931	0.41	−1.85	0.10	73	2.87/3.15/2.14/2.47	LP	3FGL J1754.0–2930
J1753.6–2539	3.77	0.09	0.02	276	7.21/8.67/7.68/8.02	LP	3FGL J1754.0–2538
J1755.5–2511	4.39	−0.04	0.05	59	3.46/4.34/3.56/3.84	LP	...
J1758.5–2405	5.68	−0.07	0.04	95	4.89/5.52/5.06/5.58	LP	3FGL J1758.8–2402
J1759.0–2345	5.98	0.05	0.03	115	4.69/5.04/5.33/4.75	LP	3FGL J1758.8–2346
J1800.5–2359	5.99	−0.43	0.03	276	10.92/10.89/11.71/10.88	LP	3FGL J1800.8–2402
J1801.1–2313	6.69	−0.09	0.03	137	9.25/8.34/9.22/8.84	LP	...
J1801.2–2451	5.29	−0.96	0.07	47	3.01/3.70/3.75/4.34	PL	...
J1801.4–2330	6.51	−0.36	0.02	234	14.26/13.28/13.65/12.17	LP	...
J1801.6–2358	6.13	−0.64	0.04	29	2.40/2.86/2.62/3.18	PL	...
J1802.2–3043	0.29	−4.05	0.05	32	0.75/0.80/0.67/0.71	PL	3FGL J1802.4–3043
J1808.2–3358	358.05	−6.72	0.07	51	1.33/1.35/1.15/1.41	PL	3FGL J1808.3–3357
J1809.5–2332	7.39	−2.00	0.01	7791	64.82/66.11/65.87/66.49	LP	3FGL J1809.8–2332

**Notes.**

<sup>a</sup> The localizations and  $TS$  are for the Pulsars intensity-scaled IEM, but the fluxes for each IEM are also supplied ordered as Pulsars intensity/index-scaled, OBstars intensity/index-scaled, respectively.

<sup>b</sup> Table 7 in Appendix B lists the corresponding spectral parameters for each IEM.

scaling procedure (Section 3.1), gives similar contributions by IC emission for annuli  $>1$  to the total flux over the  $15^\circ \times 15^\circ$  region for the Pulsars and OBstars IEMs. Also, for each IEM the total emission from the scaled local and outer annulus (annuli 5 and 6) across the  $15^\circ \times 15^\circ$  region is very similar.

The major difference is the distribution of the  $\pi^0$ -decay flux over annuli 2–4. The standout feature is how the H I-related  $\pi^0$ -decay flux for annuli 3 and 4 (Table 6) is correlated with the essentially complete suppression of the  $\pi^0$ -decay flux in annulus 1 for the OBstars index-scaled IEM. Similar patterns appear with the other IEMs, but are less pronounced. The

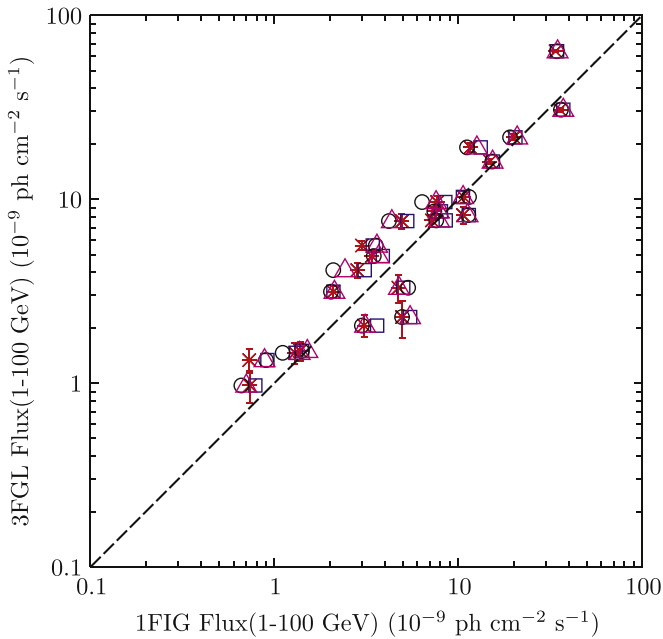


**Figure 6.** Flux of 1FIG sources associated with 3FGL sources. Symbols: crosses, Pulsars intensity-scaled; open squares, Pulsars index-scaled; open circles, OBstars intensity-scaled; open triangles, OBstars index-scaled. The dashed line is a guide for the eye.

scaling procedure results in combinations of the structured fore-/background emission that leave only a small amount of flux for the annulus  $1 \pi^0$ -decay templates to be assigned by the likelihood maximization (Section 3.2.2).

While the IC and combined point source fluxes are larger than the formal statistical uncertainties, and the variation across IEMs, this is not true for the annulus  $1 \pi^0$ -decay emission. For this component the reliability of the fluxes obtained is uncertain: the intrinsic variation of the structured fore-/background across IEMs is large in comparison, and there is also a potential correlation with some of the flux attributed to the point sources, which is discussed further below.

#### 4.2. Point Sources

Table 3 summarizes the properties of the 48 point sources ordered by increasing right ascension over the  $15^\circ \times 15^\circ$  region with  $TS \geq 25$  for the Pulsars intensity-scaled IEM, which was the model used for the point-source positions and localization uncertainties. The list is termed the first *Fermi* Inner Galaxy point source catalog (1FIG). 27 of the 1FIG sources have a 95% containment localization error ellipse that intersects the 95% containment radius of a 3FGL point source. These associations are also given in the table. The correlation plot (Figure 6) shows that the fluxes of the 1FIG sources compared with their associations in the 3FGL are in good agreement.

Fourteen sources in the 3FGL have a multi-wavelength association. For example, the 3FGL source J1701.2-3006 is associated with the globular cluster NGC 6266. For the given  $TS \geq 25$  detection threshold used for 1FIG source detection 10 counterparts in the 3FGL are obtained that have a multi-wavelength association. The W28 supernova remnant (3FGL J1801.3-2326e) is included in the model of the region as an extended source (see Section 3.2.1), while the 3FGL sources J1716.6-2812 (NGC 6316), J1746.3-2851c

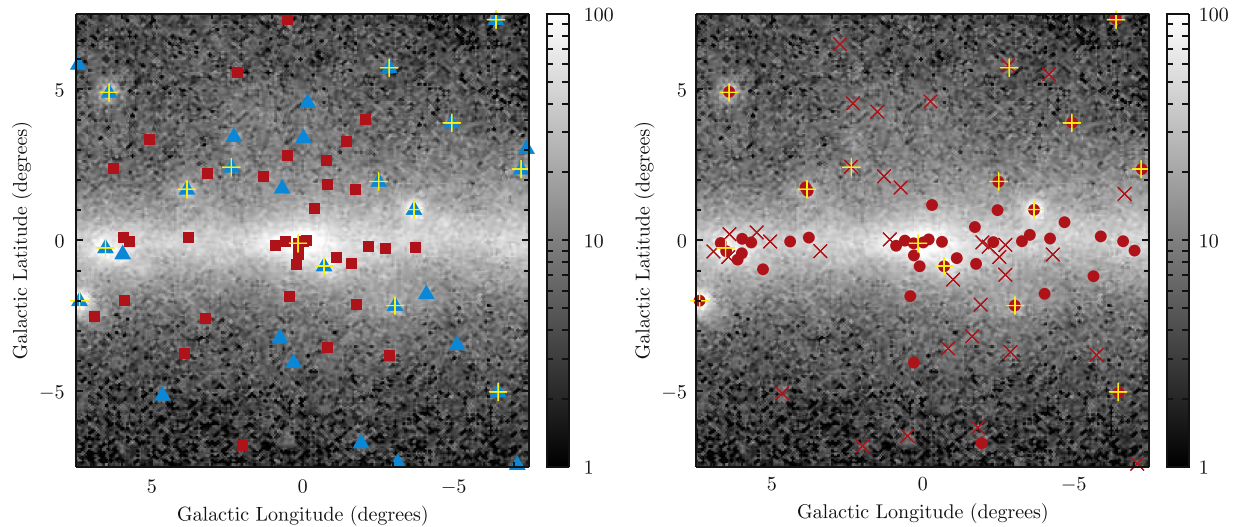
(PWN G0.13-0.11), and J1750.2-3704 (Terzan 5) are missing from 1FIG. The latter missing counterparts are discussed in Section 5.2, together with possible multi-wavelength associations for other 1FIG sources.

Figure 7 shows the point sources from the 1FIG and 3FGL overlaid on the total photon counts for the  $15^\circ \times 15^\circ$  region about the GC. The 3FGL sources are separated according to whether they have an analysis flag set in the 3FGL catalog: flagged sources indicate their properties depend on the IEM or other details of the analysis in the region. The density of flagged 3FGL sources is higher out of the Galactic plane than that of the 1FIG sources, even if the  $TS < 25$  source candidates are included. This can be partly attributed to differences in the treatment of the IC emission, and its interplay with the gas components, for the IEMs employed for the respective analyses. The 3FGL IEM uses an all-sky IC map based on a GALPROP calculation, with its spatial distribution taken as a fixed template and the spectral parameters adjusted to improve the correspondence with the data (Acero et al. 2015a). The decomposition of the IC intensity map into Galactocentric annulus templates employed here for the first time introduces additional degrees of freedom that can account for Galactocentric radial gradients in the IC emissivities. This allows more flexibility to fit for a spatial distribution of IC emission that is not correctly represented by the baseline GALPROP calculations.

The 3FGL source density is higher out of the Galactic plane compared to the 1FIG, while the reverse is the case closer to the plane. The 1FIG sources in the plane do cluster in approximately the same regions as the high-density clusters for the 3FGL: near the W28 supernova remnant and the GC. Outside these regions the density of sources is higher than the 3FGL. That many of these additional sources appear to trace features in at least one of the annulus 1 templates is suggestive that they may be misattributed interstellar emission. This can be seen in Figure 8 where the 1FIG sources are overlaid on the fitted components of the interstellar emission for annulus 1 for the Pulsars intensity-scaled IEM. By way of example, many of the  $TS > 25$  sources appear to trace the edge of the fitted neutral gas  $\pi^0$ -decay template. Because many of these sources lack a multi-wavelength association it is not straightforward to determine whether they are true point sources.

The combined flux of 1FIG point sources and point source candidates across the  $15^\circ \times 15^\circ$  region for the Pulsars intensity-scaled IEM  $> 1$  GeV is  $44.6 \pm 1.4 \times 10^{-8} \text{ ph cm}^{-2} \text{ s}^{-1}$ . Of this total, only 20% is due to point sources with a multi-wavelength association in the 3FGL, while 10% of the total is due to  $TS < 25$  source candidates. Focussing on the region  $-7.5 \leq l \leq -0.5$ ,  $-1.5 \leq b \leq 1.5$  (the region with the highest density of 1FIG sources without 3FGL counterparts and where they appear to trace the edge of the  $\pi^0$ -decay template), the combined flux from the  $TS > 25$  1FIG sources is  $\sim 20\%$  of the total point-source flux over the  $15^\circ \times 15^\circ$  region. The total flux for the annulus 1  $\pi^0$ -decay along the entire plane from the fit is about the same as that from these sources alone.

Although the absolute values differ similar relative contributions to the total point source flux determined for each of the other IEMs are obtained. However, for the Pulsars index-scaled, and both OBstars IEM variants, the annulus 1  $\pi^0$ -decay template is even less intense than for the Pulsars



**Figure 7.** Point sources for 3FGL (left panel) and 1FIG (right panel, for Pulsars intensity-scaled IEM) overlaid on the total counts for the  $15^\circ \times 15^\circ$  region about the GC. Left panel symbol key: filled squares, “flagged” 3FGL sources; filled triangles, other 3FGL sources; upright crosses, 3FGL sources with a multi-wavelength association. Right panel symbol key: filled circles, 1FIG sources with  $TS \geq 25$ ; angled crosses, 1FIG source candidates with  $TS < 25$ ; upright crosses, as in left panel. Color scale is in counts per  $0.05^2$  degree pixel.

intensity-scaled IEM. Over all IEMs, the 17 1FIG sources with  $TS > 100$  have a variation in the combined flux that is  $\lesssim 1\%$ . For sources without a 3FGL multi-wavelength association and with 1FIG  $TS$  in the range  $25 \leq TS < 100$  (24 sources) the combined flux over this region is more strongly dependent on the IEM:  $6.7\text{--}8.3 \times 10^{-8} \text{ ph cm}^{-2} \text{ s}^{-1}$ . The larger of these values is comparable to the variation to the total fore-/background for the IEMs over this region (Table 2).

It is probable that there is some misattribution of interstellar emission to low-flux (e.g., less than  $\sim \text{few} \times 10^{-9} \text{ ph cm}^{-2} \text{ s}^{-1} > 1 \text{ GeV}$ ) point sources. The low-flux sources are all relatively low-significance sources and modeled using power-law spectra (Section 3.2.1). The distribution of their spectral indices over the  $15^\circ \times 15^\circ$  region may provide some information: softer spectral indices (e.g.,  $\gtrsim 2.5$  in spectral index) can indicate that the low-flux sources are more likely associated with the structured/gas-related interstellar emission, while harder indices can indicate a more “IC-like” distribution. Figure 9 shows all point sources and candidates with a  $TS < 50$  overlaid on the fitted  $\pi^0$ -decay annulus 1 template for the Pulsars intensity-scaled IEM. The point sources are coded according to the spectral indices: circles show those with indices  $> 2.5$ , while triangles show those with indices  $\leq 2.5$ . There is no clear trend of softer spectrum point sources tracing the structured emission, nor one where the harder spectrum point sources have a high density out of the plane. It is difficult to identify the exact fraction of the emission, or to what component (gas-related, IC), the low-flux point sources could be ascribed if they are indeed due to mismodeling of the interstellar emission over the region.

### 4.3. Residuals

Figure 4 shows the fractional residuals below the differential flux spectrum for each IEM integrated over the  $15^\circ \times 15^\circ$  region as a function of energy. Some trends are evident: each model over-predicts the data below  $\sim 2 \text{ GeV}$  and under-predicts above  $\sim 2 \text{ GeV}$ , except for the Pulsars index-scaled IEM that over-predicts the data  $\gtrsim 5 \text{ GeV}$ .

Figure 10 shows the longitude and latitude profiles for the energy ranges<sup>80</sup> 1–1.6, 1.6–10, and  $> 10 \text{ GeV}$  for the Pulsars index-scaled model shown in Figure 4, which has the lowest fractional residual across the 1–100 GeV energy range. (The features are mostly the same for the other IEMs with the major difference their magnitude in terms of counts, hence these profiles are not shown because of their similarity.)

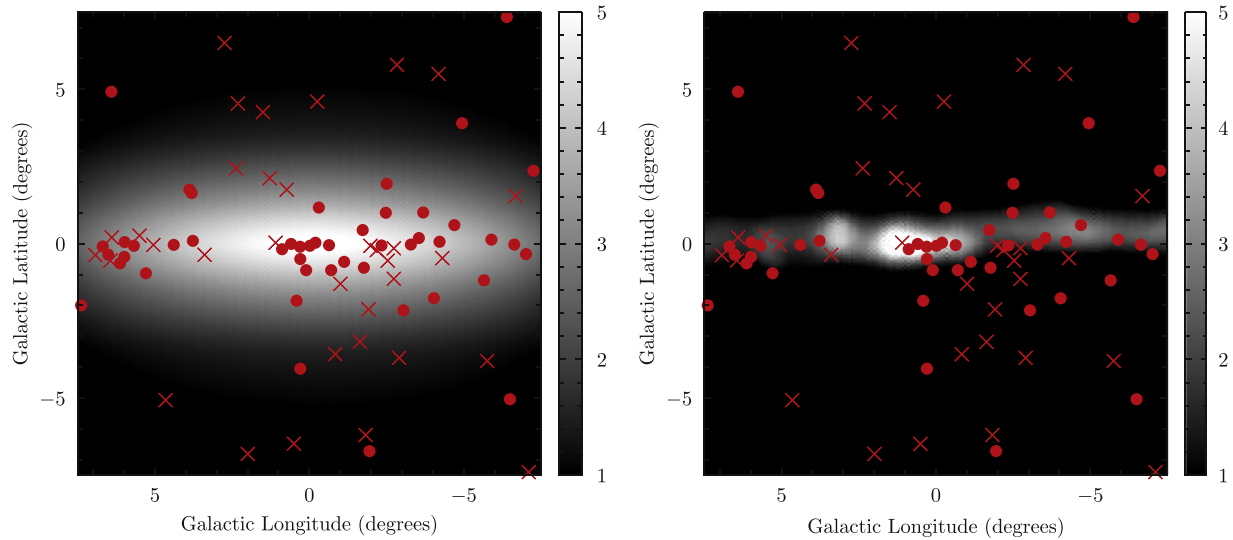
The lower sub-panel for each figure gives the residual counts ( $data - model$ ). While there is considerable statistical noise, the total residual counts may be distributed asymmetrically in longitude about the GC below 10 GeV. However, quantifying such an asymmetry using a purely data-driven method, e.g., by forming the ratio  $A = (f_+ - f_-)/(f_+ + f_-)$  where  $f_+$  and  $f_-$  are the counts for some equally sized regions about some symmetry line, is not useful here because the residuals are of mixed sign.

Figure 11 shows in greater detail the spatial distributions of the residual for each of the IEMs and in the three energy bands. Common features across IEMs are present: the model is too bright compared to the data mostly along the Galactic plane for the lowest energy band (1–1.6 GeV) and this behavior is more pronounced for the intensity-scaled IEMs, while the models under-predict the data around the GC in the 1.6–10 GeV energy band.

Note that the ecliptic crosses the  $15^\circ \times 15^\circ$  region and therefore the Sun and Moon contribute to the observed emission Abdo et al. (2011). The emissions from these objects are not included in the fore-/background models employed in this analysis. But above 1 GeV it is small relative to the observed residual emission.<sup>81</sup>

<sup>80</sup> Each band approximately covering the energy intervals where the under-/over-predictions in the fractional residuals are more prominent. Note that the profiles are essentially the same even if, e.g., a smaller latitude band is used to construct the longitude profiles because the majority of counts are concentrated near the plane.

<sup>81</sup> The solar  $\gamma$ -ray flux  $> 1 \text{ GeV}$  within  $5^\circ$  of the Sun track on the sky is  $\sim 2 \times 10^{-8} \text{ ph cm}^{-2} \text{ s}^{-1}$  (Abdo et al. 2011), while the Lunar  $\gamma$ -ray flux  $> 1 \text{ GeV}$  is  $\sim 2 \times 10^{-9} \text{ ph cm}^{-2} \text{ s}^{-1}$  (Abdo et al. 2012). The fraction of the data taking period spent in the  $15^\circ \times 15^\circ$  region by either object is  $\sim 5\%$  of the total, and their emission is distributed about the ecliptic. For the Sun this corresponds to  $\sim 50\text{--}100$  counts  $> 1 \text{ GeV}$ , which is  $\lesssim 0.1\%$  of the total counts. The Lunar contribution is lower.



**Figure 8.** Point sources from 1FIG overlaid on the fitted components (Section 3.2.2) of the interstellar emission from annulus 1 for the Pulsars intensity-scaled IEM. Left panel shows the overlay on the annulus 1 IC while the right panel shows the overlay on the annulus 1  $\pi^0$ -decay components from atomic and molecular gas. Symbol key: filled circles, 1FIG sources with  $TS > 25$ ; angled crosses, 1FIG sources candidates with  $TS < 25$ . Color scale is in counts per  $0.05^2$  degree pixel.

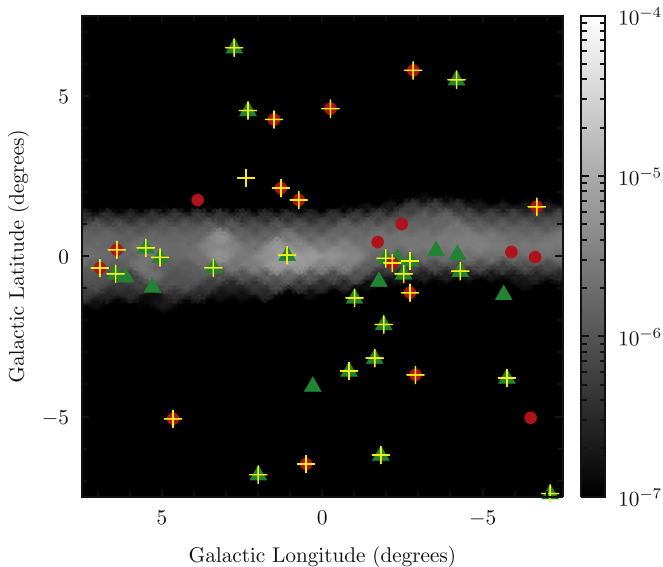


**Figure 9.** Sources and source candidates with  $TS < 50$  overlaid on the fitted  $\pi^0$ -decay emission from annulus 1 for the Pulsars intensity-scaled IEM. Symbol key: filled circles, sources and source candidates with power-law indices  $> 2.5$ ; filled triangles, sources and source candidates with power-law indices  $\leq 2.5$ ; crosses, source candidates with  $TS < 25$ . The highest flux  $> 1$  GeV for a point-source shown is  $3.7 \times 10^{-9}$  ph  $\text{cm}^{-2} \text{s}^{-1}$ . Color scale units:  $\text{cm}^{-2} \text{s}^{-1} \text{sr}^{-1}$ .

Although the spatial distribution of the residuals is not suggestive of a contribution by the *Fermi* bubbles, it is also possible that there is some emission from them over the  $15^\circ \times 15^\circ$  region. Without a spatial template for the *Fermi* bubbles over the region their contribution is tested using a model with an isotropic spatial distribution across the  $15^\circ \times 15^\circ$  region with intensity and spectrum as determined from analyses at higher latitudes (e.g., Ackermann et al. 2014). The *data – model* agreement only marginally improves if this contribution is included.

The model over-prediction at the lowest energies is primarily correlated with the Galactic plane, which could be due to mismodeling of the gas component of the IEMs. Some of the positive residual in the few GeV range could be due to an

extended component that is more concentrated toward the GC compared to the IEM components. But, the profiles shown in Figure 10 and the spatial distributions shown in Figure 11 represent the situation if the fit is made only for interstellar emission about the GC and point sources. As a consequence it is difficult to establish properties for an additional component not presently included in the model for the region. A spatial and spectral model needs to be assumed and fit to the data together with the interstellar emission and point sources.

A set of templates for the spatial distribution of the additional component is selected with each fit together with the interstellar emission components and point sources using the maximum-likelihood procedure described above. Because the excess emission in the few GeV range is distributed around the GC, templates that peak there are considered. A set of two-dimensional Gaussians with varying HWHM ( $1^\circ$ ,  $2^\circ$ ,  $5^\circ$ ,  $10^\circ$ ) are used. While these spatial distributions do not have an obvious physical interpretation, they can be used to gauge the radial extent of the positive residuals. Spatial templates to model the predicted distribution for  $\gamma$ -rays produced by DM particles annihilating or decaying in the Galaxy are included. The inner region of the Galaxy is predicted to be the brightest site for a DM signal in  $\gamma$ -rays and could be well within the sensitivity of *Fermi*-LAT. To model the DM density distribution, the Navarro, Frenk, and White (NFW) (Navarro et al. 1997) profile is employed<sup>82</sup> with different choices for the slope of the profile in the innermost region,  $\gamma = 1, 1.2$ . The NFW profile is predicted by simulations of cold DM, while the more peaked distribution with  $\gamma = 1.2$  (NFW-c) is motivated by earlier work (e.g., Hooper & Goodenough 2011; Abazajian & Kaplinghat 2012) and could arise when baryonic effects are included in simulations. The square of the NFW profile is used as a template for DM annihilation, hereafter referred to as simply the “NFW profile.” The possibility that an unresolved

<sup>82</sup> The following parametrization is employed:  $\rho(r) = \rho_0 \left( \frac{r}{R_s} \right)^{-\gamma} \left( 1 + \frac{r}{R_s} \right)^{-3}$ , where  $\gamma$  is the slope of the DM distribution in the innermost region and its value is discussed in the text. As for the other parameters, in this work  $R_s = 20$  kpc and  $\rho_0$  corresponds to a local DM density  $\rho_\odot = 0.3 \text{ GeV cm}^{-3}$ .

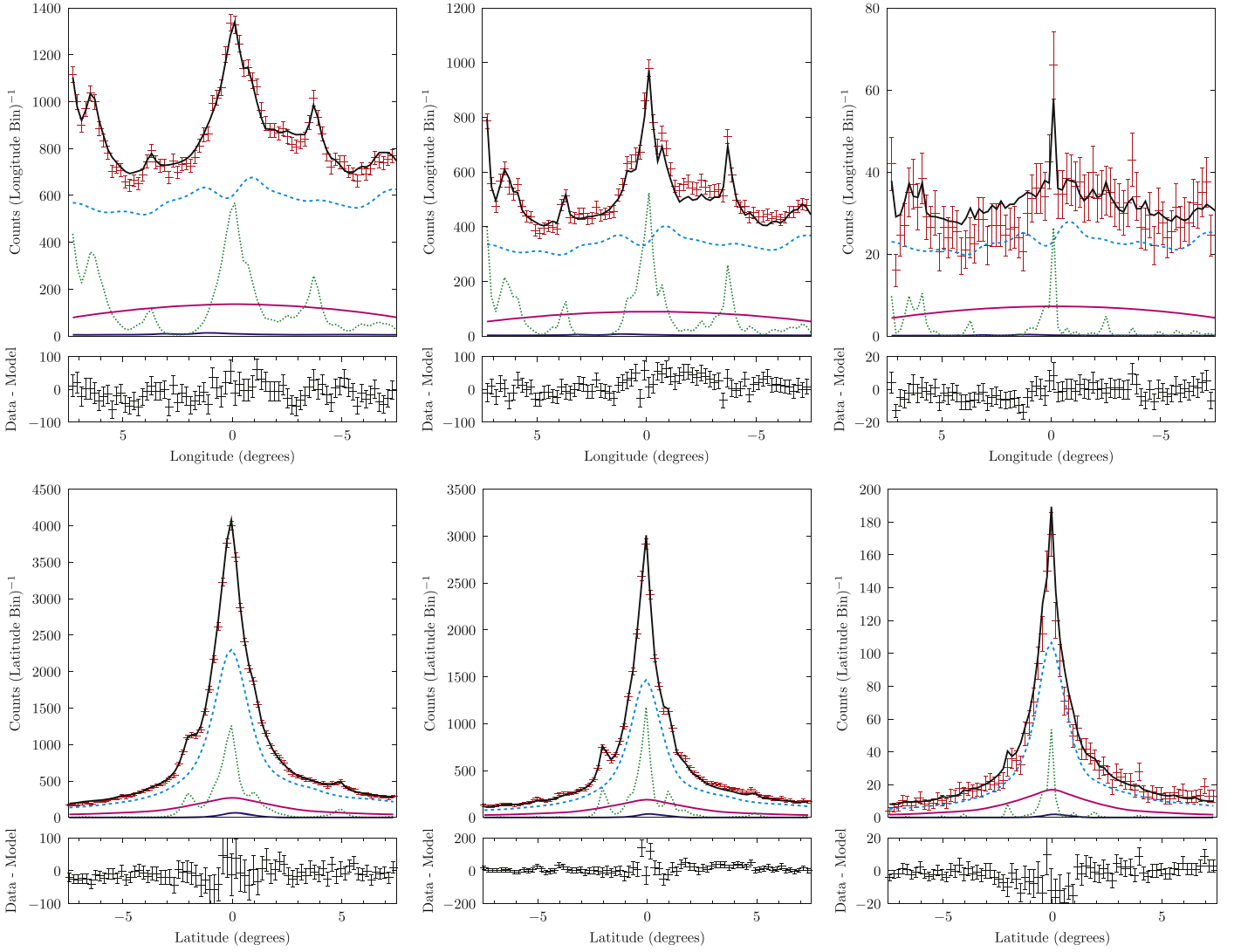


**Figure 10.** Longitude (upper) and latitude (lower) profiles for 1–1.6 (left), 1.6–10 (middle), and 10–100 GeV energies (right), respectively, of the residual counts (data – model) for the Pulsars index-scaled IEM after fitting for interstellar emission and point sources across the  $15^\circ \times 15^\circ$  region. Line styles: black/solid, total model; cyan/dashed, fore/background interstellar emission; green/dotted, point sources; magenta/solid, IC from annulus 1; blue/solid,  $\pi^0$ -decay from annulus 1. Point styles: red, data; black, residual counts. The lower sub-panel for each profile gives the residual counts after the model has been subtracted from the data. The error bars are statistical. Profiles for the residuals counts for other IEMs display similar features with the major difference being the number of counts.

population of  $\gamma$ -ray point sources such as pulsars distributed along the Galactic plane is contributing to the observed emission is also considered. Predictions of the  $\gamma$ -ray emission from unresolved pulsars exist and they span a range of possibilities (e.g., Story et al. 2007; Faucher-Giguère & Loeb 2010). Here, the spatial distribution of an unresolved pulsar population is modeled using the distribution of the CO gas in annulus 1, because this is a likely tracer for regions of high-mass star formation, and smooth it with a  $2^\circ$  Gaussian to account for the scale height of the associated pulsar population.

For each of the spatial templates listed above, the spectrum is modeled with an exponential cut-off power law. This form has some flexibility to model a pulsar or a DM annihilation spectrum without supposing specific scenarios. For each of the spatial templates listed above and for each of the IEMs, a maximum-likelihood fit is made in the  $15^\circ \times 15^\circ$  region as described in Section 3.2.2.

The improvement in likelihood as well as the resulting best-fit parameters for the spectrum of the additional component are

summarized in Table 4.<sup>83</sup> All templates yield statistically significant improvements compared to the model without the additional component. The largest improvements are observed for the NFW annihilation templates, whereas the unresolved source component yields the smallest improvements.

The new component spectra present harder spectral indices and lower energy cutoffs for the index-scaled IEMs compared to the intensity-scaled variants. This is consistent with the index-scaled models having overall better agreement with the data at higher energy, and therefore attributing the positive residual found for the intensity-scaled IEMs  $\gtrsim 10$  GeV to gas related emission rather than to the new component. Within the same IEM, the spectrum for the more peaked templates (NFW and NFW-c for DM annihilation, and the  $1^\circ$  Gaussian) present softer indices and higher energy cutoffs. The NFW decay and the  $10^\circ$  Gaussian (the more extended templates) perform similarly to each other for most IEMs.

<sup>83</sup> 500 MeV is the lowest value of the energy cutoff allowed in the fit.

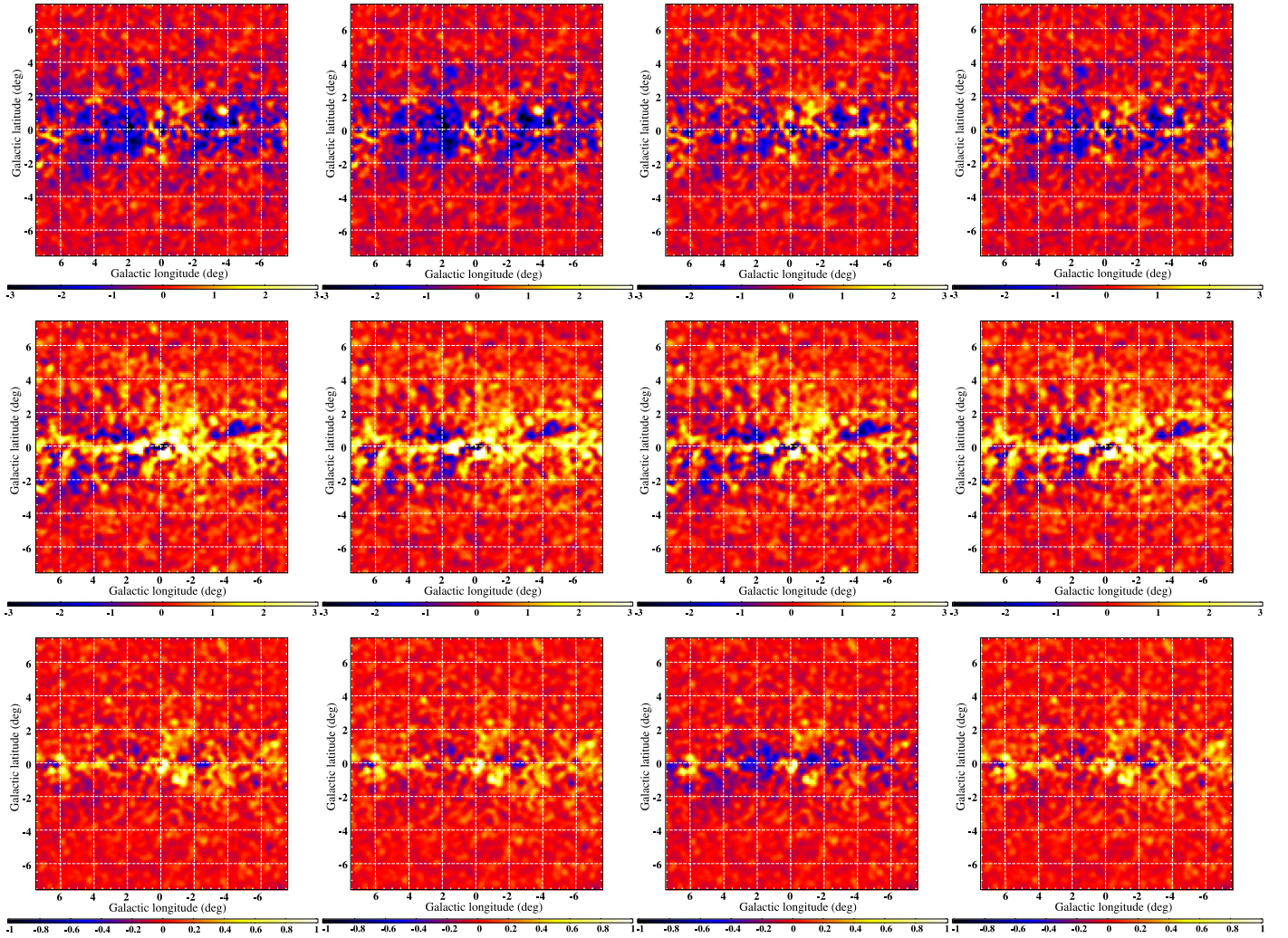


**Figure 11.** Residual counts for the  $15^\circ \times 15^\circ$  region about the GC for the Pulsars and OBstars IEMs for energy ranges 1–1.6 GeV (upper row), 1.6–10 GeV (middle row), and  $>10$  GeV (bottom row). The two leftmost columns show the residual counts for the intensity-scaled variant for the Pulsars and OBstars, respectively. The two rightmost columns show the residual counts for the index-scaled variant for the Pulsars and OBstars, respectively. The color scale is in counts/0.1 deg<sup>2</sup> pixel.

Among the Gaussian templates, the  $2^\circ$  and  $5^\circ$  gaussians perform better for the Pulsar IEMs, while the  $5^\circ$  and  $10^\circ$  gaussians for the OB stars IEMs. This result is an indication that the Gaussian templates might be compensating for mismodeling of the IC contribution, whose morphology differs for the OB stars and Pulsars IEMs.

By including the NFW profile component the agreement with the data has an overall improvement for all the models up to  $\sim 30$  GeV, as shown in Figure 12, with the Pulsars index-scaled variant yielding the best agreement over the full energy range. However, a broad range for the best-fit parameters of the spectral model is found. The variation is not easily ascribed to a covariance with only a single component of the model that is fitted over the  $15^\circ \times 15^\circ$  region. For example, the annulus 1 IC and H I-related  $\pi^0$ -decay normalizations adjust in the fit to compensate for the additional template. But the spectral parameters of the residual template are not solely determined by the fit with the interstellar emission components and point sources over the inner region about the GC; the fore-/background interstellar emission has an effect as well.

The intensity-scaled IEMs yield similar spectral parameters for the NFW template, but the results for the index-scaled IEMs have a stronger variation. This can be seen in Figure 13, which shows the flux spectral envelopes from including the uncertainties on the normalization and spectral index obtained for the NFW template for the 4 IEMs. The index-scaled IEMs have the distinction of harder spectra for the  $\pi^0$ -decay interstellar emission for annuli 2–4 (Table 5), but also modified IC contributions for annuli 2 and 3 compared to their intensity-scaled counterparts. The majority of the  $\pi^0$ -decay fore-/background interstellar emission is due to annulus 4 and, as already noted in Section 4.1, even small variations in the structured fore-/background interstellar emission can have a follow-on effect on the spatial distribution of the residual emission over the  $15^\circ \times 15^\circ$  region. It is difficult to test how small variations in the  $\pi^0$ -decay fore-/background from this annulus affect the residual model parameters because the annulus 4 fit parameters are determined at an intermediate step in the fitting. But the comparison between the results for the Pulsars and OBstars index-scaled IEMs show that the different spectral parameters obtained for the structured interstellar

**Table 4**  
Residual Component Fit Parameters

IEM Model	Spatial Template	Spectral Index	Cut-off Energy (MeV)	$\Delta \log L$	$\log L$
<b>Pulsars</b>					
intensity-scaled	NFW annihilation	$-1.5 \pm 0.1$	$16360 \pm 2945$	282	-83027
	NFW-c <sup>a</sup> annihilation	$-1.4 \pm 0.1$	$13120 \pm 2075$	272	-83037
	NFW decay	$2.5 \pm 0.4$	$1012 \pm 130$	99	-83210
	1 <sup>ob</sup>	$-1.6 \pm 0.1$	$20210 \pm 7451$	118	-83191
	2 <sup>ob</sup>	$-0.4 \pm 0.5$	$3804 \pm 1706$	157	-83152
	5 <sup>ob</sup>	$-0.1 \pm 0.7$	$2999 \pm 1470$	154	-83155
	10 <sup>ob</sup>	$3.3 \pm 0.5$	$819 \pm 100$	85	-83224
	Unresolved sources	$0.7 \pm 1.0$	$2313 \pm 1350$	84	-83225
<b>Pulsars</b>					
index-scaled	NFW annihilation	$0.2 \pm 0.3$	$1346 \pm 177$	165	-82757
	NFW-c annihilation	$0.5 \pm 0.1$	$1132 \pm 30$	166	-82755
	NFW decay	$4.1 \pm 0.4$	$500 \pm 4$	67	-82854
	1 <sup>o</sup>	$0.0 \pm 1.1$	$1241 \pm 641$	76	-82846
	2 <sup>o</sup>	$2.0 \pm 0.2$	$693 \pm 31$	100	-82822
	5 <sup>o</sup>	$2.3 \pm 2.0$	$684 \pm 356$	101	-82820
	10 <sup>o</sup>	$4.1 \pm 0.5$	$500 \pm 8$	59	-82862
	Unresolved sources	$3.3 \pm 0.3$	$500 \pm 2$	36	-82885
<b>OBstars</b>					
intensity-scaled	NFW annihilation	$-1.5 \pm 0.1$	$18100 \pm 2939$	298	-83163
	NFW-c annihilation	$-1.3 \pm 0.1$	$12610 \pm 2062$	236	-83225
	NFW decay	$-0.9 \pm 0.3$	$10540 \pm 6265$	159	-83302
	1 <sup>o</sup>	$0.3 \pm 1.7$	$2348 \pm 2426$	23	-83438
	2 <sup>o</sup>	$0.6 \pm 1.7$	$2251 \pm 2076$	80	-83381
	5 <sup>o</sup>	$-1.2 \pm 0.2$	$12680 \pm 3860$	213	-83248
	10 <sup>o</sup>	$0.2 \pm 0.1$	$3001 \pm 207$	144	-83317
	Unresolved sources	$0.1 \pm 0.6$	$3513 \pm 1543$	74	-83387
<b>OBstars</b>					
index-scaled	NFW annihilation	$-0.5 \pm 0.5$	$2682 \pm 912$	165	-82819
	NFW-c annihilation	$-0.4 \pm 0.4$	$2528 \pm 696$	148	-82836
	NFW decay	$3.5 \pm 0.5$	$664 \pm 74$	102	-82882
	1 <sup>o</sup>	$1.1 \pm 0.2$	$1057 \pm 68$	42	-82942
	2 <sup>o</sup>	$3.4 \pm 0.7$	$644 \pm 102$	58	-82926
	5 <sup>o</sup>	$1.9 \pm 2.4$	$962 \pm 695$	118	-82866
	10 <sup>o</sup>	$3.8 \pm 0.5$	$625 \pm 69$	96	-82888
	Unresolved sources	$4.7 \pm 0.7$	$500 \pm 7$	28	-82956

#### Notes.

<sup>a</sup> NFW-contracted profile with index  $\gamma = 1.2$ .

<sup>b</sup> Two-dimensional Gaussian with corresponding half-width, half-maximum.

emission fore-/background can alter the final fitted values for all components over the  $15^\circ \times 15^\circ$  region.<sup>84</sup>

With the interstellar emission fore-/background held constant for each IEM, the interplay between the centrally peaked positive residual template and the interstellar emission components is not surprising. Because the IC component is maximally peaked toward the GC for all IEMs an additional template that is also peaked there will also be attributed some flux when fit. Over all IEMs the effect of including the NFW

model for the residual results in an IC annulus 1 contribution that is up to three times smaller and H I annulus 1 contribution that is up to three times larger.

Note that even if a centrally peaked template is included as a model for the positive residual, it does not account for all of the emission. This can be seen in Figure 14, which shows the residual counts for the NFW template and IEM with the best spectral residuals (Pulsars index-scaled). Qualitatively, the remainder does not appear distributed symmetrically about the GC below 10 GeV, and still has extended positive residuals even at higher energies along and about the plane.

## 5. DISCUSSION

### 5.1. Interstellar Emission

This study is the first using the *Fermi*-LAT data that has made a separation between the large-scale interstellar emission of the Galaxy and that from the inner  $\sim 1$  kpc about the GC. The IC emission from annulus 1 is found to dominate the interstellar emission from the innermost region, and represents

<sup>84</sup> The Pulsars index-scaled IEM has the same spectral parameters across all annuli interior to the solar circle for the separate H I- and CO-components and the lowest cut-off energy for the residual template, while the OBstars index-scaled IEM has the annulus 2 and 3 components set to the GALPROP predictions because they did not converge in the IEM fitting. Whether annuli 2 and 3 have a significant effect on the residual spectral parameters for the Pulsars index-scaled IEM was tested by also setting them to the GALPROP predictions and refitting for the annulus 1 interstellar emission, point sources, and residual model parameters. The normalization and cut-off energy of the residual model did not appreciably change, indicating that the majority of any effect related to the structured fore-/background from the index-scaled IEMs is likely from annulus 4.

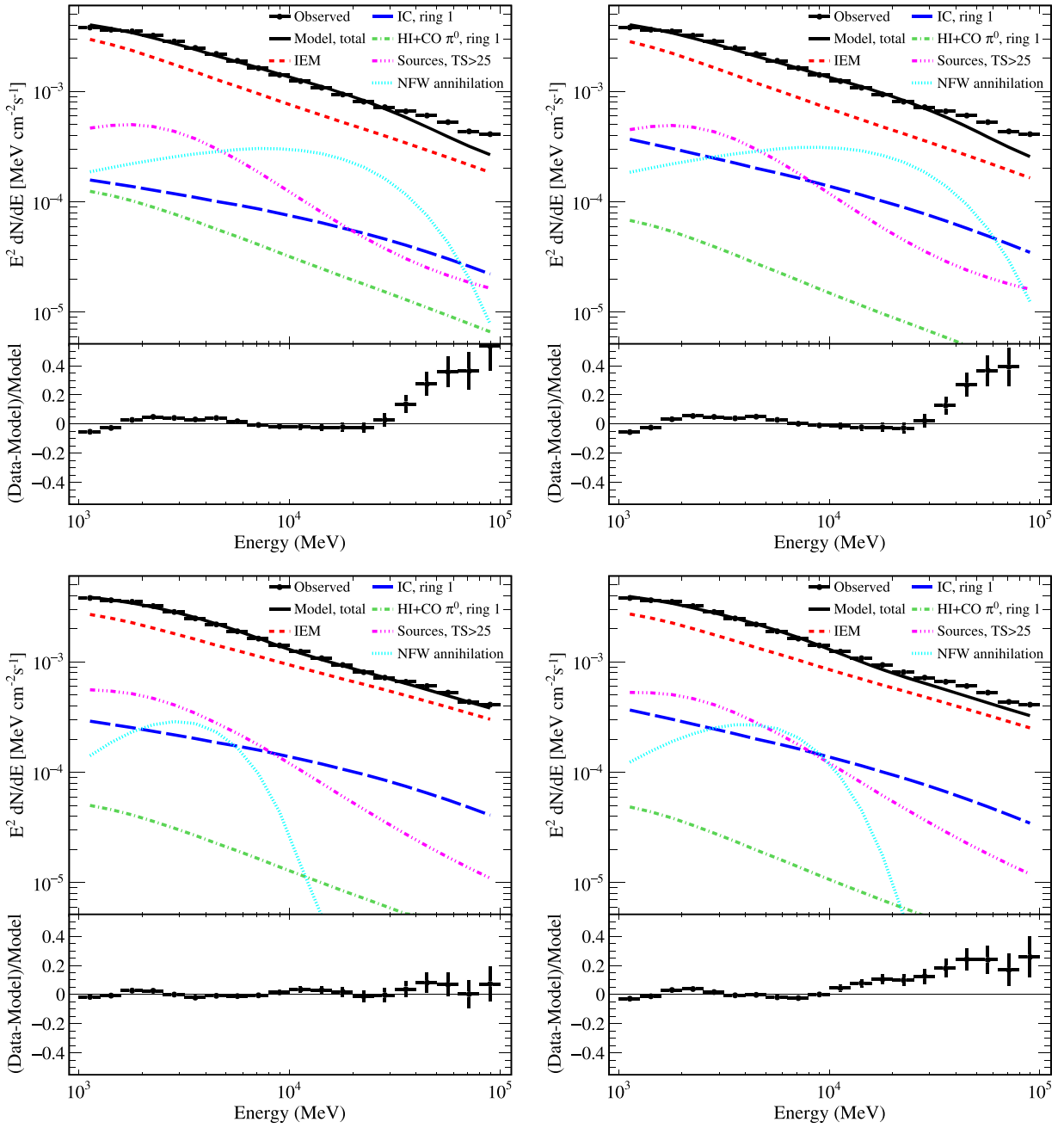


**Figure 12.** Differential fluxes for the  $15^\circ \times 15^\circ$  region about the GC for the four IEMs constrained as described in Section 3.1 using an NFW profile centered on the GC as an additional spatial template for the maximum-likelihood fit with spectrum modeled with a exponential cut-off power-law function. Upper row shows the intensity-scaled for the Pulsars (left) and OBStars (right) IEMs. Lower row shows the index-scaled for the Pulsars (left) and OBStars (right) IEMs. Line styles: solid (total model), long-dash (IC, annulus 1), dot-dash (H I and CO gas  $\pi^0$ -decay, annulus 1), dot-dot-dot-dash (point sources), dash (Galactic interstellar emission excluding annulus 1 for IC, H I and CO gas  $\pi^0$ -decay), dot (new component). Solid circles: data.

the majority of the IC brightness from this component along and through the line of sight toward the GC. The contribution by the IC from annulus 1 to the total flux depends on the IEM and whether the residual is fitted (Section 4.3). For the latter case the IC from annulus 1 is still up-scaled compared to the GALPROP predictions, but by a factor  $\sim 2$  lower than if fitted solely for the interstellar emission components and point sources. The remainder is distributed across the H I-related  $\pi^0$ -decay annulus 1 component and the template used to fit the residual centered on the GC. For either case (residual template used/not-used), the fitted *fluxes* attributed to the IC annulus 1 component across all IEMs are within a factor  $\sim 2$ —the flux

and its range is the important quantity, instead of the individual (model-dependent) scaling factors.

The Pulsars intensity-scaled IEM with the residual template gives the minimal “enhanced” flux for IC annulus 1. The average CR electron intensity  $\gtrsim 5$  GeV in the Galactic plane is estimated for this model within  $\sim 1$  kpc of the GC as  $\sim 2.8 \pm 0.1 \times 10^{-4} \text{ cm}^{-2} \text{ s}^{-1} \text{ sr}^{-1}$ , where the uncertainty is statistical only. This energy range is used because its lower bound corresponds to the CR electron energies producing  $\sim 1$  GeV IC  $\gamma$ -rays. This is  $\sim$  a factor of two higher than the local total CR electron density for this same energy range for the Pulsars baseline model. On the other hand, the OBStars

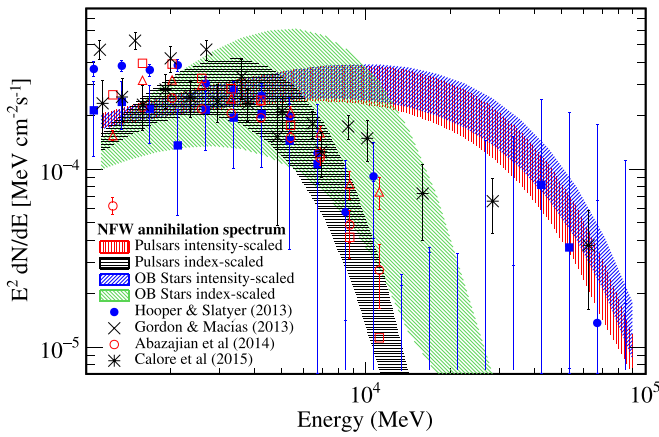


**Figure 13.** Differential fluxes for the  $15^\circ \times 15^\circ$  region about the GC of the NFW component with spectrum modeled with an exponential cut-off power law. The envelopes include the fit uncertainties for the normalization and spectral index. Hatch styles: Pulsars, intensity-scaled (red, vertical); Pulsars, index-scaled (black, horizontal); OB Stars, intensity-scaled (blue, diagonal-right); OB Stars, index-scaled (green, diagonal-left). Results from selected other works are overlaid. Filled symbols: Hooper & Slatyer (2013), different symbols bracket the results obtained when different regions of the sky are considered in the fit; Angled crosses: Gordon & Macias (2013); Open symbols: Abazajian et al. (2014), front-converting events shown with triangles, front- and back-converting events shown with squares and circles, depending on the modeling of the fore-/background. Stars: Calore et al. (2015a). Note: the overlaid results are rescaled to the DM content over the  $15^\circ \times 15^\circ$  region for an NFW profile with index  $\gamma = 1$ .

intensity-scaled IEM fitted without the residual component gives the maximal “enhanced” flux for IC annulus 1. The average CR electron intensity  $\gtrsim 5$  GeV in the Galactic plane within  $\sim 1$  kpc of the GC for this IEM is  $\sim 9.4 \pm 0.1 \times 10^{-4} \text{ cm}^{-2} \text{ s}^{-1} \text{ sr}^{-1}$ .

Measurements of the interstellar emission at hard X-ray energies to MeV  $\gamma$ -rays by *INTEGRAL*/SPI (Bouchet et al. 2011) show that the majority is due to IC scattering by  $\sim$ GeV energy CR electrons off the infrared component of the ISRF.<sup>85</sup> The GALPROP calculations, which follow the same “conventional” model normalization condition to local CR measurements as used in this paper, made to interpret the SPI measurements indicate that IEMs with at least factor of two higher CR densities toward the inner Galaxy are a plausible explanation for the data. Another possible explanation is a higher intensity for the radiation field energy density in the inner Galaxy than used in the standard ISRF model of Porter et al. (2008); these possibilities are not tested here because they require detailed investigations that are beyond the scope of the current work. The higher CR electron densities obtained from this analysis are plausible given the same electrons are IC scattering different components of the ISRF to produce the interstellar emission  $\gtrsim 1$  GeV and at SPI energies.

The purpose for fitting the baseline IEMs to the data was to obtain estimates for the interstellar emission fore-/background. However, the fit results for the individual rings for each IEM potentially give some information on the large-scale distribution of CRs throughout the Galaxy. Tables 5 and 6 in Appendix A.1 give the fit coefficients and fluxes for the scaled IEMs, while Figure 15 shows the integrated fluxes for the 1–10 (top) and 10–100 GeV (bottom) energy ranges, respectively, over the  $15^\circ \times 15^\circ$  region for the GALPROP-predicted and

scaled version of each IEM for the Pulsars (left) and OBstars (right) source distributions.

The fitting procedure generally increases the intensity of each annulus relative to the nominal model. The coefficients for the intensity-scaled Pulsars and OBstars IEMs are mostly higher than the GALPROP predictions toward the inner Galaxy (annuli 2–3). Those for the OBstars IEM are higher than the Pulsars, which reflects the fact that the spatial distribution for the CR sources in this model cuts off within  $\sim 2$  kpc of the GC. The cut off in the OBstars source spatial distribution produces a *predicted* CR intensity that is lower compared to the Pulsars IEM over this region. The fitting procedure adjusts the OBstars predictions upward more than the Pulsars to compensate. This indicates that a Pulsars-style spatial source distribution is closer to the real spatial distribution of sources within  $\sim 2$  kpc of the GC. But, even the Pulsars spatial source distribution is scaled up by the fit over this region, indicating that even more “peaked” source models, or some modification to the propagation model, is required to describe the distribution of CRs toward the inner Galaxy. Meanwhile, there is more similarity in the scaling coefficients for annuli 4–6. This reflects that the CR source distributions and propagation conditions for both IEMs are not significantly different in their Galactocentric radial distributions in these annuli.

The spectral parameters for the annuli interior to the solar circle for the index-scaled variants give results that are strongly dependent on the IEM being fit. For the Pulsars IEM the spectrum of the CR nuclei/gas interstellar emission is consistently harder across annuli 2–4 for both CO and H I components than the intensity-scaled IEMs. For the OBstars IEM only the H I component has a hardening to the spectrum across annuli 2–4. For this IEM the fits for annuli 2–3 were unstable when fitting both CO and H I components. Because the size of the regions are small, the low flux of the annuli 2–3 components in comparison to those that are already-determined from fitting to the outer longitude ranges means that the data are insufficiently constraining. However, a convergent fit is obtained if the CO-related  $\pi^0$ -decay templates is set to the GALPROP prediction. The motivation for allowing the additional freedom to fit the spectrum for the gas-related interstellar emission interior to the solar circle is solely to improve the fit residuals. But, the harder index for the H I and CO component when fitting the Pulsars IEM can be an indication that the assumption of a uniform CR source spectrum across the Galaxy is insufficient, or that the diffusive propagation of CRs is non-uniform.

Generally, the fitting results can be interpreted as a reconfirmation that the CR gradient in the Galaxy is flatter than expected based on current knowledge of the Galactocentric radial distribution of CR sources, which has been known since the SAS-2 (Stecker & Jones 1977), COS-B (Bloemen et al. 1986; Strong et al. 1988), and EGRET (Hunter et al. 1997; Digel et al. 2001) all-sky surveys. The explanation is not clear. Bloemen et al. (1993) suggested that the radial distribution of CR sources derived from observations may be biased and their real distribution is flatter or the diffusion parameters derived from the local CR measurements are not the same throughout the Galaxy. Solutions to this issue in terms of CR propagation phenomenology have been proposed: CR-driven Galactic winds and anisotropic diffusion (Breitschwerdt et al. 2002), or non-uniform diffusion coefficient that increases

<sup>85</sup> The majority of the IC  $\gamma$ -rays in the energy range of this study are produced by scattering off the optical component of the ISRF.

**Table 5**  
Scaling Coefficients with Respect to the Baseline IEM

Model	Process	Annulus 2	Annulus 3	Annulus 4	Annulus 5	Annulus 6
<b>Pulsars</b>						
intensity-scaled	IC	1.3	1.3	1.6	1.49	1.8
	$\pi^0$ -decay H I	1	1	1.62	1.21	1.74
	CO	1	1	1.42	1.4	0.3
<b>Pulsars index-scaled</b>						
	IC	1.71	1.71	1.6	...	...
	$\pi^0$ -decay H I	(0.5, 0.29, 0.14) <sup>a</sup>	(0.5, 0.29, 0.14)	(0.32, 0.29, 0.14)	...	...
	CO	(0.22, 0.30, 0.30)	(0.22, 0.30, 0.30)	(0.37, 0.30, 0.30)	...	...
<b>OBstars</b>						
intensity-scaled	IC	4.15	4.15	1.48	1.13	1
	$\pi^0$ -decay H I	3.7	3.7	1.2	1.19	1.41
	CO	1.2	0.8	1.3	1.37	0.69
<b>OBstars index-scaled</b>						
	IC	2.21	2.21	1.48	...	...
	$\pi^0$ -decay H I	(1, 0.17, 0.17)	(1, 0.4, 0.4)	(0.67, 0.17, 0.17)	...	...
	CO	1	1	(0.17, 0.41, 0.06)	...	...

**Note.**

<sup>a</sup> Tuple entries refer to parameters for Equation (1): ( $f_0$ ,  $\gamma_1$ ,  $\gamma_2$ ).

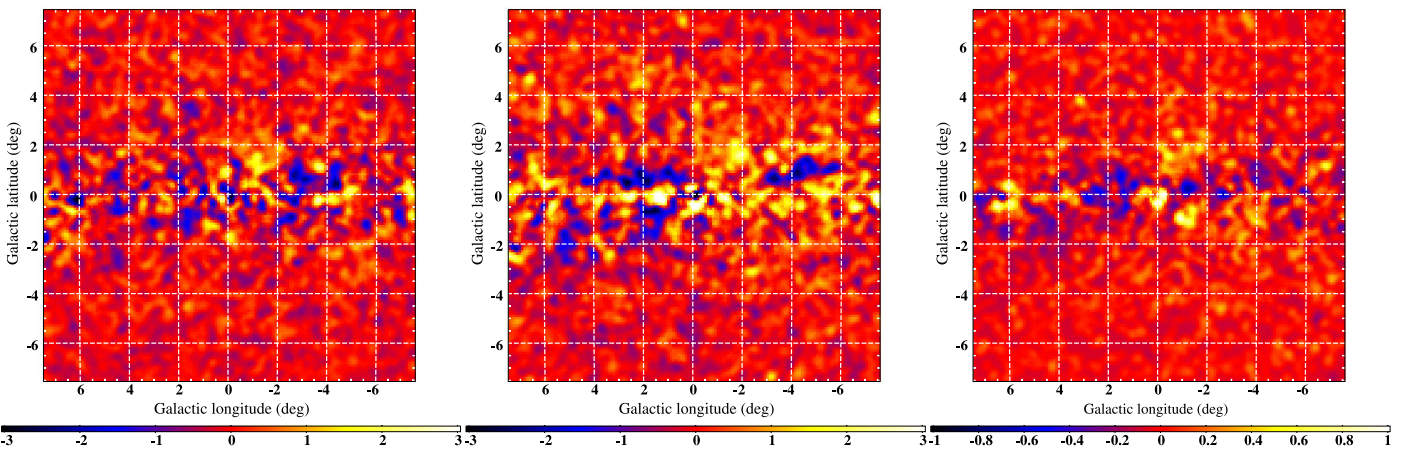


**Figure 14.** Residual counts for the  $15^\circ \times 15^\circ$  region about the GC for the Pulsars index-scaled IEM together with the NFW profile template for energy ranges 1–1.6 GeV (left), 1.6–10 GeV (middle), and  $>10$  GeV (right). The color scale is in counts/0.1 deg<sup>2</sup> pixel.

with Galactocentric radius and the distance from the Galactic plane (Shibata et al. 2007).

The current analysis has focussed on finding IEMs to estimate the fore-/background toward the inner Galaxy. The broader implications of the scaled IEMs developed in this study for the large-scale distribution of CRs in the Galaxy are deferred to future work.

### 5.2. Point Sources

Figure 16 shows the 1FIG sources and source candidates overlaid on the *Fermi*-LAT data used in this paper, and 3FGL multi-wavelength associated sources, together with SNRs from Green’s SNR catalog<sup>86</sup> (Green 2014) and pulsars from the ATNF catalog<sup>87</sup> (Manchester et al. 2005), respectively, that are within 95% of the 1FIG source/source candidate error ellipse. The 3FGL sources that have likely counterparts at other wavelengths that are listed in the catalog *not* detected in the 1FIG are either due to a too low *TS* (3FGL J1716.6-2812—

NGC 6316), or are more than the 95% containment radius of the error ellipse from a potential 1FIG counterpart (3FGL J1750.2-3704—Terzan 5 and 3FGL J1746.3-2851c—PWN G0.13-0.11).

There are 14 1FIG sources and source candidates with overlaps with the above mentioned SNR and pulsar catalogs. Multiple overlaps occur across and within the catalogs, e.g., SNR 354.1+00.1 and PSR J1701–3006A,D,E overlap with 1FIG J1701.1–3004.

The 1FIG source J1801.4–2330 overlaps with SNR 006.5–00.4, which has been detected in the first LAT catalog of SNRs (Ackermann et al. 2016). 1FIG J1740.1–3057 overlaps with SNR 357.7–00.1 (MSH 17–39), and has been detected previously in *Fermi*-LAT data (Castro et al. 2013). The source 1FIG J1745.5–2859 overlaps with SNR 000.0+00.0 (Sgr A East), but this is in a strongly confused region and other counterparts may be possible. The 3 other SNRs (SNR 354.1+00.1, SNR 355.4+00.7, and SNR 000.3+00.0 corresponding to 1FIG J1730.2-3351, 1FIG J1731.3–3235, and 1FIG J1746.4–2843, respectively) are new detections in high-energy  $\gamma$ -rays at *Fermi* energies. Follow-on studies are

<sup>86</sup> <http://www.mrao.cam.ac.uk/surveys/snrs/>

<sup>87</sup> <http://www.atnf.csiro.au/people/pulsar/psrcat/>

**Table 6**  
Scaled Fluxes<sup>a</sup> >1 GeV per Annuli for Each IEM Over the 15° × 15° Region

Model	Process	Annulus 2	Annulus 3	Annulus 4	Annulus 5	Annulus 6
Pulsars						
intensity-scaled	IC	9.82 <sup>b</sup>	...	17.38	1.34	0.89
	$\pi^0$ -decay H I	2.65	3.69	63.53	20.43	3.28
	CO	2.60	3.58	44.64	3.42	0.44
Pulsars						
index-scaled	IC	12.92		17.38	...	...
	$\pi^0$ -decay H I	5.27	7.33	49.86	...	...
	CO	2.43	3.34	49.38	...	...
OB-stars						
intensity-scaled	IC	11.33		16.53	1.19	0.40
	$\pi^0$ -decay H I	6.28	9.47	45.10	20.36	2.39
	CO	4.05	3.75	45.46	3.49	1.14
OB-stars						
index-scaled	IC	6.04		16.53	...	...
	$\pi^0$ -decay H I	3.82	17.59	56.85	...	...
	CO	3.37	4.69	40.90	...	...

**Notes.**

<sup>a</sup> Units:  $10^{-8}$  ph cm<sup>-2</sup> s<sup>-1</sup>.

<sup>b</sup> IC flux for annuli 2 and 3 are combined.

required to better characterize their spatial and spectral properties.

The comparison with the ATNF catalog yields 9 1FIG sources overlapping with known pulsars. The 1FIG source J1750.2–3705 is the counterpart of the globular cluster NGC 6441, which has been detected in high-energy  $\gamma$ -rays (Tam et al. 2011). Four of the remaining eight overlap with nearby pulsars ( $\lesssim 0.2$  kpc) and are listed in the LAT Second Catalog of Gamma-ray Pulsars<sup>88</sup> (Abdo et al. 2013). The remaining four sources have been identified previously and searches for pulsed emission have been made but with no detections (Abdo et al. 2013).

Obviously the comparison made here between the 1FIG sources and  $\gamma$ -ray source classes is not exhaustive. However, more than two thirds of the 1FIG sources do not have associations with sources in known classes of  $\gamma$ -ray emitters. The unassociated 1FIG sources tend to be close to the Galactic plane. It remains a significant possibility that a majority of the point sources found over the 15° × 15° region can be attributed to mis-identified interstellar emission, as already discussed in Section 4.2.

### 5.3. Residuals

A number of studies of the residual emission toward the inner Galaxy have been performed, as described in Section 1. Figure 13 compares the results from this analysis with selected results from the literature. The comparison is useful because a similar spectral model to other authors is used when fitting the residual emission associated with the centrally peaked spatial templates. The IEMs that are used in this paper are scaled to the data outside of the 15° × 15° region to reduce the discrepancies, particularly along the Galactic plane, by the a-priori GALPROP-generated IEMs from Ackermann et al. (2012a). The developments also made as part of this work have allowed additional degrees of freedom to be included for the scaling of the IEMs—treating the IC template as the sum of individual templates with the same Galactocentric radial boundaries as the

$\pi^0$ -decay templates, and allowing for spectral variations in the  $\pi^0$ -decay templates from those predicted interior to the solar circle—that go beyond the modeling of the interstellar emission employed by other analyses (e.g., Calore et al. 2015b). In addition, a catalog of point sources is derived for each IEM that is used in the analysis of the inner region about the GC. The prescriptive method of determining the fore-/background interstellar emission, together with the self-consistent treatment of the point sources<sup>89</sup> and interstellar emission for the inner  $\sim$ kpc about the GC allows the least biased estimate to-date to be made of the positive residual emission about the GC. This work finds that for individual IEMs the spectral parameters for a spatial template that peaks at the GC, such as the NFW profile, can be relatively tightly constrained. However, over all IEMs considered in this work the variation of, for example, the cut-off energy for an exponential power-law spectral model is much wider than that for any individual model.

Although the spectral residuals are generally improved by an additional template, discrepancies remain that are more pronounced for the intensity-scaled variants of the IEMs. It should be emphasized that despite this observation the intensity-scaled IEMs cannot be excluded on the basis of fits made to the 15° × 15° region about the GC. All four of the IEMs are tuned to data outside this relatively small region, providing similar improvements to the all-sky residuals, and hence are equivalent representations of the fore-/background toward and through the GC. Because of the limitations in modeling the interstellar emission, the higher energy cutoff spectra for the NFW profile component with the intensity-scaled IEMs cannot be ruled out. With the limited freedom for the interstellar emission components (only the normalization for the IC, H I and CO-related  $\pi^0$ -decay intensity maps are allowed to vary—three parameters) and in the specification of the spectral model for the positive residual (normalization, spectral index, and cut-off energy—three parameters) the spread in the positive residual template parameters is considerable (see above.) If more freedom is allowed for the spectrum of the positive residual then the spectral residuals for

<sup>88</sup> [http://fermi.gsfc.nasa.gov/ssc/data/access/lat/2nd\\_PSR\\_catalog/](http://fermi.gsfc.nasa.gov/ssc/data/access/lat/2nd_PSR_catalog/)

<sup>89</sup> Note: this includes the sub-threshold point source candidates and those that satisfy the  $TS > 25$  criterion for “detection” used for the 1FIG.

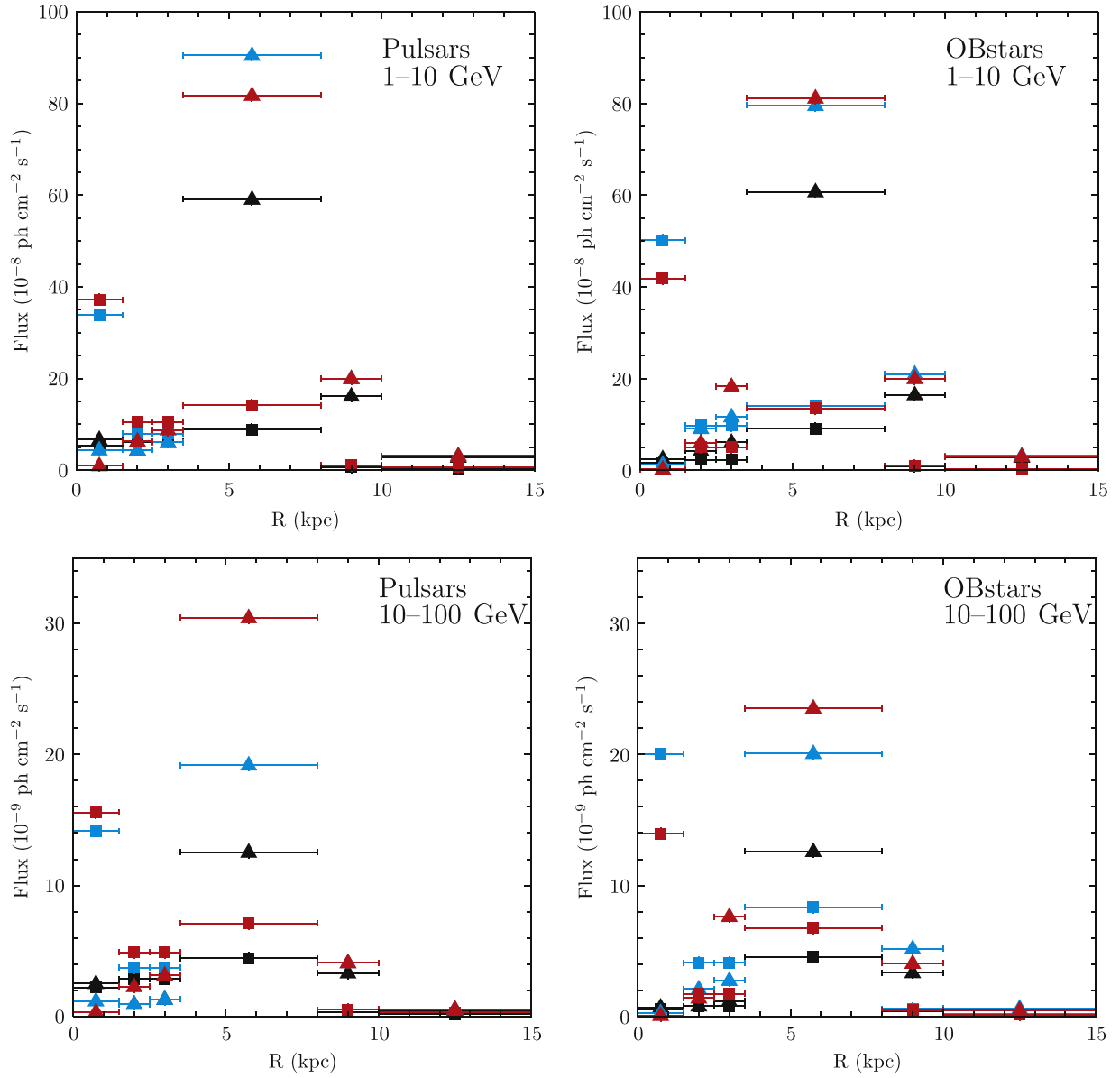


**Figure 15.** Flux per ring for the  $15^\circ \times 15^\circ$  region about the GC for the Pulsars (left) and OBstars (right) IEM variants for the 1–10 (top) and 10–100 GeV (bottom) energy ranges. Point colors: black, GALPROP-predicted; cyan, intensity-scaled; red, index-scaled. Point types: filled square, IC; filled triangle,  $\pi^0$ -decay. Note some symbols are obscured for annuli at larger radii because the intensity-/index-scaled variants are the same outside the solar circle.

all four IEMs over the  $15^\circ \times 15^\circ$  region can be very small. Figures 17 and 18 show the results for all IEMs if more degrees of freedom are allowed to model the spectrum of the NFW profile<sup>90</sup> (note that the feature at  $\sim 40$  GeV is not significant when the fit uncertainties are considered, as shown in Figure 18). For this choice of spectral model indeed the residuals are very good for all IEMs. It is therefore premature, because of the variations in the IEMs and their limitations, to favor a specific IEM among those we considered and to attribute the high energy residual to a particular origin.

Although a large formal statistical significance may be indicated for the detection of a new component, note that fitting a centrally peaked profile does not account for all of the

positive residual over the  $15^\circ \times 15^\circ$  region. Ascribing a singular origin to such a residual component is premature given the limited constraints on the other emission components over the  $15^\circ \times 15^\circ$  region. A complete assessment of the uncertainties (see Section 5.4) is required to understand the nature of its spatial and spectral parameters. The current work demonstrates that even in the optimistic scenario where the presence of a DM component in the data might be established based on the spatial distribution of the associated  $\gamma$ -ray emission, important information on the DM particle such as its mass and annihilation spectrum is strongly dependent on the IEM. This was first demonstrated by Agrawal et al. (2015) using preliminary results based on this work.

#### 5.4. Limitations of the Analysis

The IEMs used in this analysis are cylindrically axisymmetric averaging the CR densities and other details azimuthally

<sup>90</sup> The spectral model is a power-law function per energy bin, with 10 bins equally spaced in logarithmic energy over the 1–100 GeV energy range. This model is defined by a normalization and spectral index in each bin, for a total of 11 parameters.

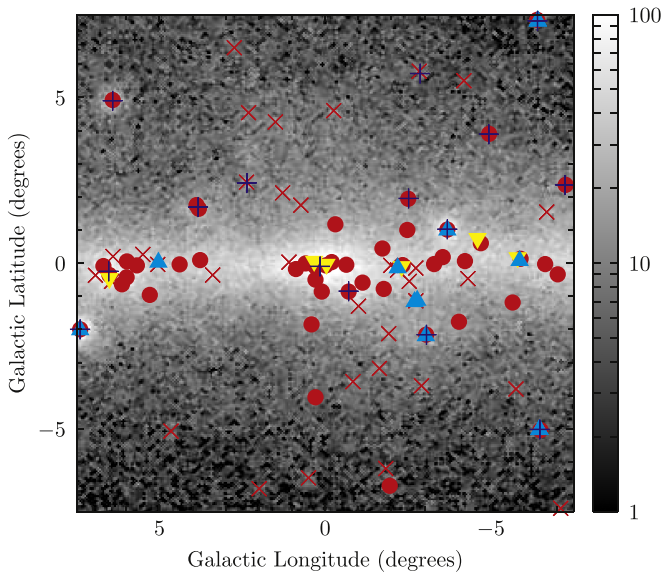


**Figure 16.** 1FIG sources and source candidates and *Fermi*-LAT data used in this paper with pulsars from the ATNF catalog (Manchester et al. 2005) and Green’s SNR catalog (Green 2014) overlaid. Symbol key: filled circles, 1FIG sources; angled crosses,  $TS < 25$  source candidates; upright crosses, 3FGL multi-wavelength associated sources; inverted triangles, SNRs from Green’s catalog with spatial overlap with a 1FIG source within its 95% error ellipse; upright triangles, pulsars from the ATNF catalog within  $3\times$  the 1FIG source error ellipse. Color scale units: counts per  $0.05^2$  deg pixel.

about the GC. Some shortcomings of these models were noted earlier (Section 3.1), particularly when fitting for the large-scale interstellar emission interior to the solar circle.<sup>91</sup> The density of CR sources and other ISM components is highest inside the solar circle and is most likely radially and azimuthally dependent, e.g., being associated with spiral arms or the Galactic bar/bulge. However, in the absence of detailed three-dimensional models for the interstellar gas, radiation field, and CR sources the axisymmetric models are the only viable method for estimating the fore-/background toward and through the line of sight to the GC.

The IEM fitting interior to the solar circle uses the tangent ranges for positive and negative longitudes to obtain parameters for the annuli 2–4 (Table 5). To examine the effect of the azimuthal averaging, fits to the tangent ranges were made for positive and negative longitudes to gauge the difference in the parameters for the IEMs obtained when considering each separately. The scaling factors for annulus 4 obtained when fitting negative and positive longitude ranges were statistically consistent<sup>92</sup> with those found when fitting both ranges combined. For annuli 2 and 3 the fits to the positive and negative tangent longitude ranges result in scaling parameters that differ by factors up to  $\sim 2$  from each other, which is well beyond the statistical uncertainty; the average value obtained by fitting both tangent ranges together is approximately in-between for the intensity-scaled IEMs over annuli 2 and 3. For the index-scaled IEMs the spectral parameters are harder or softer than the average when using the positive/negative

<sup>91</sup> Toward the outer Galaxy the axisymmetric models are likely a very good approximation because the long propagation times for CRs to diffuse from regions with higher source density (inside the solar circle) to the outer Galaxy mean that any spatial granularity is effectively washed out.

<sup>92</sup> The average statistical uncertainty for the normalization of each interstellar emission component per annulus is  $\sim 10\%$ , except for annuli 2 and 3; see Appendix A.

tangent ranges individually for annuli 2–4. However, there is no clear trend and the over/under-prediction is not confined to a particular energy interval.

The uncertainty for the IEM fore-/background flux toward the GC due to the azimuthally averaged IEMs is difficult to quantify precisely. A minimal estimate can be made from the statistical uncertainty for the annulus 4  $\pi^0$ -decay flux for each IEM, because the fit results for the combined tangent ranges are within these uncertainties when fitted to the positive and negative ranges individually. Above 1 GeV this is  $\sim 4 \times 10^{-8}$  ph cm $^{-2}$  s $^{-1}$  for the  $15^\circ \times 15^\circ$  region about the GC across all IEMs. This is comparable to the fitted flux from annulus 1  $\pi^0$ -decay or the  $TS < 25$  point sources over the same region.

Any analysis employing the Galactocentric annulus decomposition for the gas column densities is subject to the loss of kinematic resolution for sight lines within  $l \sim \pm 12^\circ$  of the GC/anti-GC. Appendix B of Ackermann et al. (2012a) details the transformation of H I and CO gas-survey data into the column density distributions over Galactocentric annuli used in this analysis, and employed by many others. The assumptions made in the transformation for the site lines over the  $15^\circ \times 15^\circ$  region about the GC have an impact on the interstellar emission and point sources in the maximum-likelihood fitting and consequently the spatial distribution of residuals. Approximations made interpolating the gas column density across the  $l \pm 10^\circ$  range can result in an incorrect gas density distribution along the line of sight. Spurious point sources in the analysis and structure in residuals can result from this because a higher/lower CR intensity compared to where the gas should be placed is used in creating the interstellar emission templates. The scaling procedure for the IEM then adjusts the individual annuli potentially producing low-level artifacts due to a combination of the effects described above.

To obtain an estimate of the uncertainties associated with misplacement of the gas new maps of the column density per annuli are created. 10% of the H I gas column density is randomly displaced over the annuli and recombined with the  $\pi^0$ -decay emissivity<sup>93</sup> in each annulus to create modified intensity maps for this process, which are summed to produce new fore-/background intensity maps. The 68% fractional change per pixel from 100 such realizations for each IEM is compared with the fore-/background resulting from the scaling procedure (Section 3.1). Depending on the IEM and energy range, variations from 1% to 15% in the intensity per pixel for the fore-/background from the structured interstellar emission across the  $15^\circ \times 15^\circ$  region are obtained, with the largest for OBstars index-scaled and smallest for the Pulsar intensity-scaled IEM, respectively. Because of the somewhat arbitrary choice of the precise fraction of H I column density<sup>94</sup> that is redistributed over the annuli these variations are illustrative rather than providing a true “systematic uncertainty” associated with the gas misplacement. Note that the uncertainty is maximized toward the GC because it is furthest away from the gas column density interpolation base points at  $l \sim \pm 12^\circ$ .

<sup>93</sup> The contribution by CO-related  $\pi^0$ -decay emission is the same as that obtained from the scaling procedure.

<sup>94</sup> Similar modifications of the CO column density distribution are not explored because the detailed knowledge to make a truly informed estimate is not available.

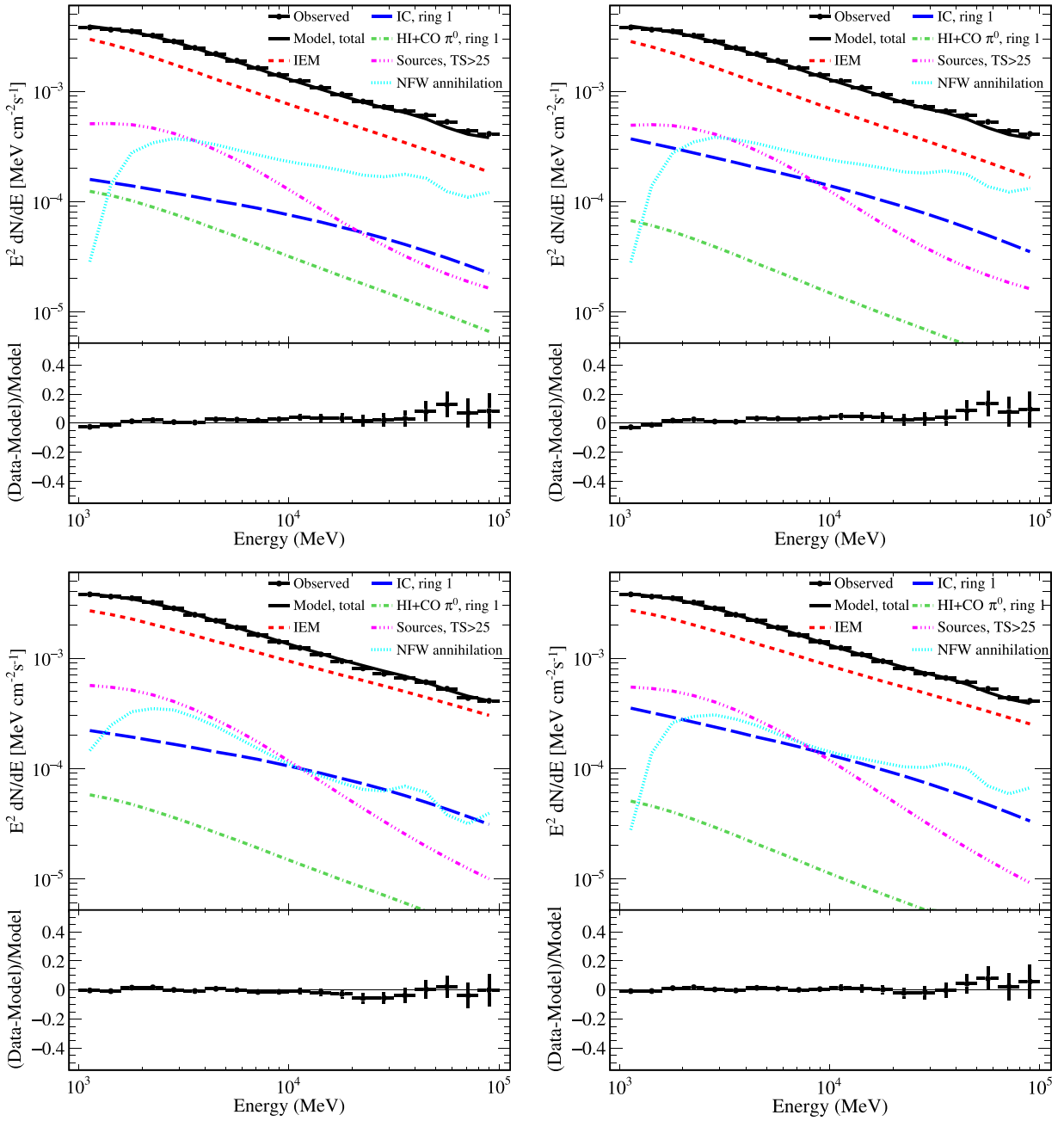


**Figure 17.** Same as in Figure 12, but with the spectrum of the NFW profile modeled with a power-law per energy band over the 1–100 GeV range.

## 6. SUMMARY

The analysis described in this paper employs specialized IEMs that are fit to the  $\gamma$ -ray data without reference to the  $15^\circ \times 15^\circ$  region about the GC. Finding point-source seeds for the same region using a method that does not rely on detailed IEMs, the source-seeds and IEMs are combined in a maximum-likelihood fit to determine the interstellar emission across the inner  $\sim 1$  kpc about the GC and point sources over the region. The overwhelming majority of  $\gamma$ -ray emission from the  $15^\circ \times 15^\circ$  region is due to interstellar emission and point sources. To summarize the results for these aspects of the analysis:

1. The interstellar emission over the  $15^\circ \times 15^\circ$  region is  $\sim 85\%$  of the total. For the case of fitting only “standard” interstellar emission processes and point sources the

fore-/background is  $\sim 80\%$  with the remaining  $\sim 20\%$  mainly due to IC from the inner region. The contribution by the  $\pi^0$ -decay process over the inner region is much less than the IC, with the relative contributions by the H I- and CO-related emission suppressed compared to the GALPROP predictions. With this scenario there are residual counts that are distributed with some general peak around the GC. If a model for the positive residual with a spatial distribution that peaks near the GC is simultaneously fit with interstellar emission and point sources, the IC flux is reduced by a factor  $\sim 3$  and the H I-related  $\pi^0$ -decay is increased by a factor  $\sim 3$ . Even with the additional parameters introduced by a model for the positive residual the IC flux is considerably enhanced compared to those predicted by the baseline IEMs, and remains the dominant interstellar emission component

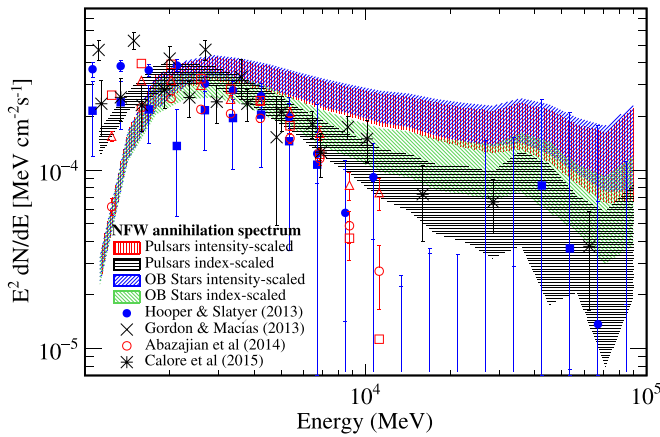


**Figure 18.** Same as in Figure 13, but with the spectrum of the NFW profile modeled with a power law per energy band over the 1–100 GeV range. The envelopes include the fit uncertainties for the normalization and spectral indices.

over the inner region about the GC. This indicates that the CR electron and/or ISRF intensities in the region are higher than those in the baseline IEMs.

2. The total flux of point sources over the  $15^\circ \times 15^\circ$  region is 15% of the total flux over the four IEMs, and this is stable whether or not a model for the residual counts is included in the fitting procedure. Only  $\sim 20\%$  of this is attributed to point sources with a 3FGL counterpart with a multi-wavelength association. Approximately 60% of the 1FIG sources have a 3FGL counterpart, with a good correlation between the 1FIG and 3FGL fluxes. However, the spatial density of 1FIG sources is more closely distributed near the Galactic plane than the 3FGL. The 1FIG contains 11 out of the 14 3FGL sources with a multi-wavelength association but the parameters of the spectral model for each vary according to the IEM that is employed. The three sources with a multi-wavelength association in the 3FGL not included in the 1FIG are either due to a  $TS$  below the detection threshold, or because they are more than the 95% containment radius of the error ellipse from a potential 1FIG counterpart. In addition, sources listed in other *Fermi*-LAT derived catalogs of SNRs and pulsars (Abdo et al. 2013; Ackermann et al. 2016), and other individual analyses are found. Spatial overlaps for 3 1FIG sources with SNRs listed in Green’s catalog (Green 2014) are obtained. These are previously undetected, but further characterization of their spatial and spectral properties in  $\gamma$ -rays awaits more detailed follow-up analyses.

A critical aspect of this analysis is the determination of point source localizations, fluxes, and spectral properties for each IEM. Over the  $15^\circ \times 15^\circ$  region spatial distribution of the source density differs between the 1FIG and 3FGL. The IEMs constructed for the present analysis employ similar gas maps to the 3FGL IEM, but use a different fitting methodology. The IEMs are not optimized to flatten residual features across the  $15^\circ \times 15^\circ$  region, and allow for more freedom to fitting the IC intensity distribution.

Many of the 1FIG point sources lie close to the Galactic plane. Although there is no definitive tracing of individual interstellar emission components by these point sources, there is a possibility that a fraction of them are misattributed

interstellar emission. The spatial distribution of point sources and point-source candidates are essential pieces of information for understanding the contribution of unresolved source populations across the region. Better quantification of the misattributed fraction is necessary to determine the correct spatial distribution of point sources over the region. However, this is beyond the scope of the current analysis.

The separation of the fore-/background interstellar emission employed in this work is not without its limitations. But, the major ones that should be investigated for an improved analysis of the high-energy  $\gamma$ -ray emission from this region are described.

The residual flux in the  $15^\circ \times 15^\circ$  region only becomes significant with respect to the interstellar emission components and point sources for energies  $\gtrsim 2$  GeV. If only interstellar emission and point sources are fit to the data the residual emission is weakly asymmetric about the GC, but the statistical noise is large. This may be suggestive of an excess in the data that is not symmetric with respect to the GC. However, the extended over-subtraction and the paucity of point sources in the region around  $l \sim 2^\circ$  are indicative of mismodeling of the interstellar emission in that region, possibly due to inadequacies in the treatment of interstellar gas along and through the line of sight toward the region. Because of this uncertainty, it cannot presently be established if this feature is caused by an asymmetric excess in the data due to something other than standard astrophysical production mechanisms.

If a model for the positive residual that uses a spatial template that is centrally peaked toward the GC with an exponentially cut-off power-law spectrum is fit together with the interstellar emission and point sources, the spectral parameters are tightly constrained. However, this analysis shows that the range of spectral parameters using such a model for the positive residual is much wider when considering multiple IEMs. Flat spectral residuals across the whole 1–100 GeV energy range are only obtained for an IEM with a significant modification to the spectra of the structured component of the interstellar emission fore-/background, compared to a GALPROP model normalized to local CR spectra. Otherwise, the spectral residuals are flat only up to  $\sim 30$  GeV.

The analysis described in this paper contrasts with other works examining the  $\gamma$ -ray emission observed by the *Fermi*-LAT toward the GC because multiple specialized IEMs are developed to estimate the fore-/background without reference to the data in the region of interest about the GC. The self-consistent determination of point sources and point-source candidates using these specialized IEMs is another element of the analysis that has previously not been employed. After subtraction of interstellar emission and point sources, an extended residual is present. It can be fit with a centrally peaked profile with a specified spectral model, but not all of the positive residual is accounted for by such a model. The flux obtained using the centrally peaked profile is comparable to that from other analyses. But the uncertainty on its spectral properties due to the interstellar emission and point source modeling means that a precise physical interpretation of its origin is premature.

The *Fermi*-LAT Collaboration acknowledges generous ongoing support from a number of agencies and institutes that have supported both the development and the operation of the

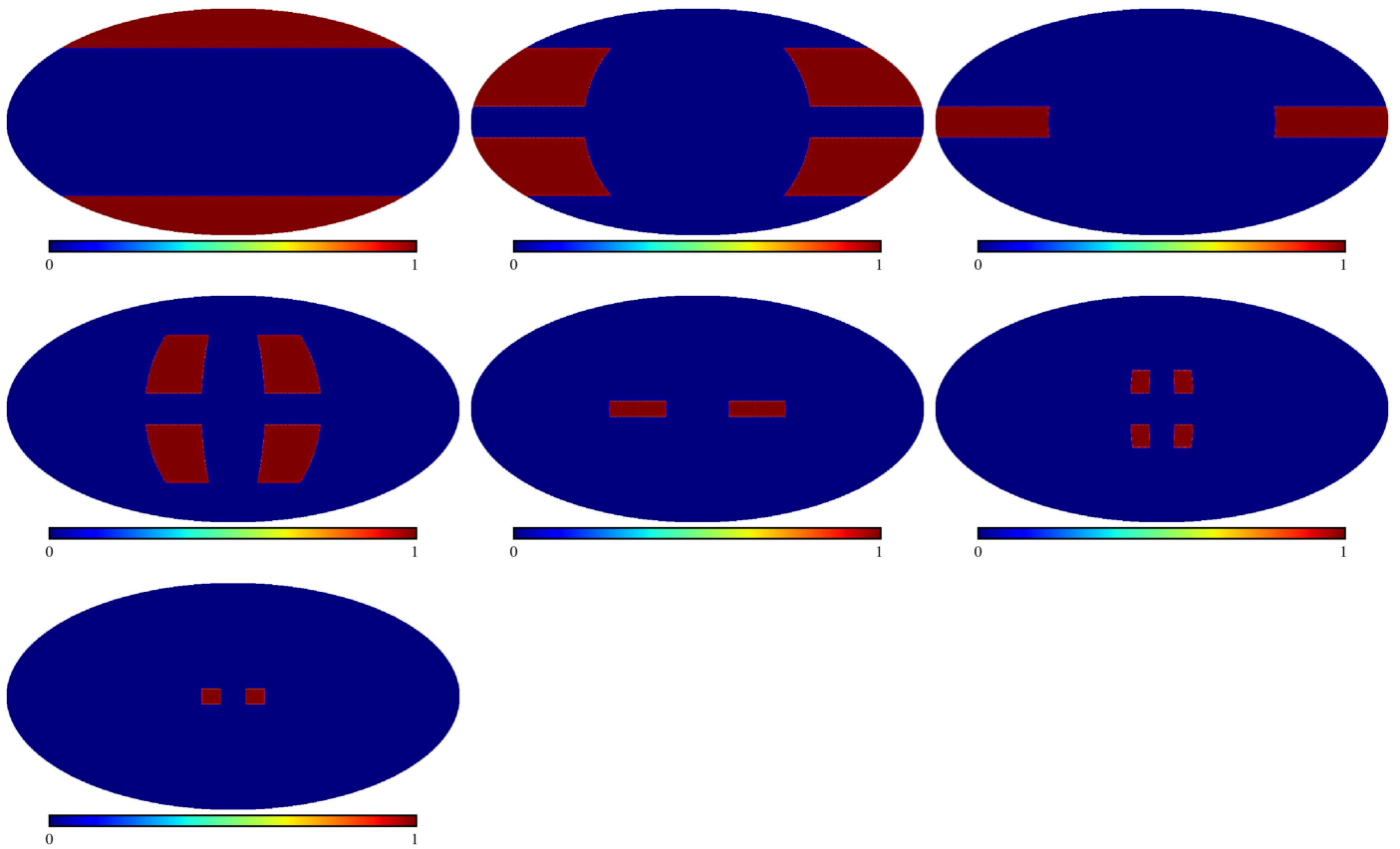


**Figure 19.** Sky regions used for fitting the IEMs. The fitting sequence follows left-to-right, top-to-bottom where a non-zero value shows the active region used for each step of the procedure. See the text for a description of the steps.

LAT as well as scientific data analysis. These include the National Aeronautics and Space Administration and the Department of Energy in the United States, the Commissariat à l’Energie Atomique and the Centre National de la Recherche Scientifique/Institut National de Physique Nucléaire et de Physique des Particules in France, the Agenzia Spaziale Italiana and the Istituto Nazionale di Fisica Nucleare in Italy, the Ministry of Education, Culture, Sports, Science and Technology (MEXT), High Energy Accelerator Research Organization (KEK) and Japan Aerospace Exploration Agency (JAXA) in Japan, and the K. A. Wallenberg Foundation, the Swedish Research Council and the Swedish National Space Board in Sweden.

Additional support for science analysis during the operations phase is gratefully acknowledged from the Istituto Nazionale di Astrofisica in Italy and the Centre National d’Études Spatiales in France.

GALPROP development is partially funded via NASA grants NNX 09AC15G, NNX 10AE78G, and NNX 13AC47G.

Some of the results in this paper have been derived using the HEALPix (Górski et al. 2005) package.

## APPENDIX A IEM SCALING PROCEDURE

The sky is sub-divided into regions where individual annuli for the different emission processed calculated by the GALPROP code have high signal-to-noise contributions. For the structured interstellar emission, the contributions by the Bremsstrahlung and  $\pi^0$ -decay from CR nuclei interacting with

ionized hydrogen in the ISM, and the Bremsstrahlung contribution from the neutral gas, are held constant throughout the scaling procedure at their respective GALPROP predictions. These are sub-dominant compared to those of CR nuclei interacting with the neutral gas and it was found in trial fits that the scaling procedure typically set these contributions to zero, which is unrealistic.

Figure 19 shows the decomposition of the sky that is used for the IEM tuning. For each of baseline IEMs described in Section 3.1 the coefficients for the per-annulus intensity maps are fit following the sequence described below.

The isotropic component for each IEM is determined first by fitting it to the data for  $|b| \geq 50^\circ$  with one free parameter per energy bin for its intensity. The coefficient of the local (annulus 5) H I-related  $\pi^0$ -decay is allowed to vary in the fit to account for possible high-latitude structure. The other components of the baseline IEM are held constant. The isotropic component includes residual-charged particle background and astrophysical signals that are isotropic or near-to isotropically distributed at high Galactic latitudes. The purpose of this step of the procedure is to determine the level of emission in the data that is structureless, regardless of its origin. The intensity of the isotropic component is held constant for the rest of IEM fitting procedure.

The intensities of the IC, H I- and CO-associated  $\pi^0$ -decay for the local and outer annuli (5 and 6) are obtained by fitting in latitude bands decreasing from  $|b| = 50^\circ$  to the plane in the outer Galaxy ( $90^\circ \leq l \leq 270^\circ$ ). The latitude bands are chosen so that the components being fit dominate the emission according to the baseline IEM. Once fit the intensities of the

components are held constant for the remainder of the procedure.

The local annulus IC and H I-related  $\pi^0$ -decay intensities are obtained from  $20^\circ \leq |b| \leq 50^\circ$ . The intensity for the local H I-related  $\pi^0$ -decay intensity obtained from the high-latitude region for determining the isotropic component is used as a seed value for the mid-latitude region fit. Then the local CO-associated  $\pi^0$ -decay and outer annulus IC intensities are obtained from fitting the region  $5^\circ \leq |b| \leq 20^\circ$ . The outer annulus (annulus 6) H I- and CO-associated  $\pi^0$ -decay intensities are determined from fitting to  $0^\circ \leq |b| \leq 5^\circ$ . This step of the procedure also determines the interstellar emission from the longitude range  $-70^\circ \leq l \leq 70^\circ$  by the local and outer annuli beyond the GC.

The contributions by IC, H I- and CO-associated  $\pi^0$ -decay for annuli 2–4 are determined by fitting to the “tangent” longitude ranges for each annulus, as given in Table 1. The intensities of the templates for the different emission processes are fit by decreasing annulus number. Concentrically fitting the tangent ranges inward, under the axisymmetric assumption used here, enables the remaining fore-/background interstellar emission to the inner  $\sim 1$  kpc to be estimated without including the data from the  $15^\circ \times 15^\circ$  region about the GC.

The intensities of the IC for annulus 4, the Loop-I model, and the H I-related  $\pi^0$ -decay are obtained from a fit in the latitude range  $|b| \geq 20^\circ$ . The IC is held constant and the intensities for the H I- and CO-related  $\pi^0$ -decay annulus 4 component and Loop-I model (using the intensities for the Loop-I and H I  $\pi^0$ -decay from the higher latitude fit as seed values) are found by fitting to the data for the latitude range  $|b| \leq 10^\circ$ . Because the IC is smoothly varying and the individual longitude ranges for annuli 2 and 3 are small, these are combined as a single annulus to determine the IC intensity for the longitude range  $10^\circ \leq |l| \leq 25^\circ$ . The IC intensity is fit using the latitude band  $10^\circ \leq |b| \leq 20^\circ$ . Higher latitudes are not employed because of the presence of the *Fermi* haze/“bubbles” (Dobler et al. 2010; Su et al. 2010), which are not

modeled by the GALPROP code. The H I- and CO-related  $\pi^0$ -decay intensities for annuli 2 and 3 are obtained by fitting over the respective tangent ranges for  $|b| \leq 5^\circ$  with the IC intensity obtained using the combined “annulus” held constant. This latitude band is smaller than for annulus 4 because the bulk of the gas column density for annuli 2 and 3 is within  $10^\circ$  of the mid-plane.

Table 5 lists the coefficients obtained from the scaling procedure for both intensity-scaled and index-scaled IEMs. These coefficients are applied to the GALPROP predictions for each of the Pulsars and OBstars IEMs. For entries that have a single number this is the scaling factor applied to the whole intensity map output by GALPROP. For entries with a tuple entry (e.g.,  $\pi^0$ -decay for annuli 2–4) the first number is the scaling factor for the intensity map, the second and third numbers are the changes in spectral index of the intensity map above/below the break energy. For the break function that is used for the index-scaled IEMs the following form is used:

$$f(E) = f_0 E^{\gamma_1} (0.5 + 0.5(E/E_{\text{break}})^{(\gamma_2 - \gamma_1)/\beta})^\beta \quad (1)$$

where  $E_{\text{break}} = 2$  GeV is the break energy,  $\beta = 0.2$  is the smoothing parameter with the value chosen to mitigate sensitivity to the precise value of the break energy, and  $\gamma_2 - \gamma_1$  are the change in the spectral index obtained from the fit above/below  $E_{\text{break}}$ .

The statistical uncertainties on the scaling factors are typically  $\sim 10\%$ – $20\%$  per fitting region. The scaling factors are held constant after fitting for individual angular ranges. Subsequent fits do not propagate these statistical uncertainties so that there the scaling coefficients for different annuli are not cross-correlated.

## APPENDIX B 1FIG POINT SOURCE SPECTRAL PARAMETERS

Table 7 shows the 1FIG point source spectral parameters across the 4 IEMs used in this work.

**Table 7**  
1FIG Point Source Spectral Parameters

Name 1FIG	Type	Pulsars		OBstars	
		Intensity-scaled	Index-scaled	Intensity-scaled	Index-scaled
1FIG J1701.1–3004	LP	(2.28 ± 0.21, 0.48 ± 0.24, 2.62) <sup>a</sup>	(2.30 ± 0.22, 0.47 ± 0.26, 2.62)	(2.23 ± 0.22, 0.51 ± 0.26, 2.62)	(2.29 ± 0.21, 0.48 ± 0.26, 2.62)
1FIG J1717.5–3342	LP	(2.52 ± 0.23, 0.63 ± 0.27, 0.35)	(2.70 ± 0.22, 0.50 ± 0.26, 0.35)	(2.59 ± 0.21, 0.57 ± 0.25, 0.35)	(2.67 ± 0.21, 0.50 ± 0.25, 0.35)
1FIG J1718.0–3056	PL	1.98 ± 0.25 <sup>b</sup>	2.15 ± 0.25	2.05 ± 0.23	2.09 ± 0.25
1FIG J1728.6–3433	PL	2.54 ± 0.19	3.03 ± 0.26	2.48 ± 0.18	2.81 ± 0.24
1FIG J1729.1–3502	LP	(1.81 ± 0.28, 0.81 ± 0.38, 2.82)	(2.33 ± 0.27, 0.66 ± 0.49, 2.82)	(1.80 ± 0.26, 0.78 ± 0.33, 2.82)	(2.12 ± 0.28, 0.66 ± 0.41, 2.82)
1FIG J1730.2–3351	PL	2.67 ± 0.20	3.10 ± 0.25	2.61 ± 0.19	2.91 ± 0.24
1FIG J1731.3–3235	LP	(1.53 ± 0.39, 1.41 ± 0.58, 2.19)	(2.33 ± 0.31, 1.12 ± 0.57, 2.19)	(1.50 ± 0.38, 1.39 ± 0.54, 2.19)	(2.11 ± 0.31, 1.10 ± 0.52, 2.19)
1FIG J1731.6–3001	LP	(2.28 ± 0.14, 0.07 ± 0.13, 0.52)	(2.41 ± 0.14, 0.00 ± 0.00, 0.52)	(2.26 ± 0.15, 0.09 ± 0.13, 0.52)	(2.32 ± 0.14, 0.04 ± 0.12, 0.52)
1FIG J1732.3–3131	LP	(1.87 ± 0.07, 0.82 ± 0.08, 1.91)	(2.03 ± 0.07, 0.76 ± 0.08, 1.91)	(1.86 ± 0.07, 0.83 ± 0.08, 1.91)	(1.99 ± 0.07, 0.77 ± 0.08, 1.91)
1FIG J1734.6–3228	PL	2.09 ± 0.20	2.47 ± 0.26	2.00 ± 0.20	2.15 ± 0.27
1FIG J1735.4–3030	PL	2.62 ± 0.19	2.84 ± 0.20	2.58 ± 0.19	2.75 ± 0.20
1FIG J1736.1–3150	PL	1.90 ± 0.19	2.07 ± 0.25	1.85 ± 0.19	1.95 ± 0.23
1FIG J1736.1–3422	PL	2.48 ± 0.18	2.65 ± 0.19	2.49 ± 0.16	2.60 ± 0.18
1FIG J1737.4–3144	LP	(0.82 ± 0.55, 2.42 ± 0.98, 2.15)	(1.63 ± 0.52, 2.48 ± 1.34, 2.15)	(0.37 ± 0.69, 2.77 ± 1.20, 2.15)	(1.00 ± 0.70, 3.01 ± 1.85, 2.15)
1FIG J1739.4–3010	PL	2.71 ± 0.20	3.13 ± 0.25	2.59 ± 0.24	2.93 ± 0.28
1FIG J1740.1–3057	PL	2.27 ± 0.17	2.57 ± 0.21	2.13 ± 0.19	2.42 ± 0.21
1FIG J1740.2–2834	LP	(3.80 ± 1.36, 1.41 ± 1.24, 0.36)	(4.84 ± 1.12, 1.77 ± 0.89, 0.36)	(5.00 ± 0.06, 2.77 ± 0.51, 0.36)	(5.00 ± 0.01, 2.22 ± 0.42, 0.36)
1FIG J1741.5–2538	PL	1.66 ± 0.27	1.79 ± 0.29	1.63 ± 0.27	0.00 ± 0.00
1FIG J1741.5–2054	LP	(2.79 ± 0.12, 1.67 ± 0.28, 1.73)	(2.86 ± 0.13, 1.62 ± 0.29, 1.73)	(2.79 ± 0.13, 1.64 ± 0.28, 1.73)	(2.83 ± 0.13, 1.63 ± 0.28, 1.73)
1FIG J1742.5–3318	LP	(2.06 ± 0.42, 3.08 ± 0.95, 2.11)	(2.53 ± 0.37, 2.61 ± 0.83, 2.11)	(2.01 ± 0.41, 3.09 ± 0.93, 2.11)	(2.33 ± 0.38, 2.76 ± 0.87, 2.11)
1FIG J1744.2–2930	LP	(2.21 ± 0.22, 0.42 ± 0.26, 2.56)	(2.87 ± 0.22, 0.29 ± 0.29, 2.56)	(2.13 ± 0.25, 0.47 ± 0.28, 2.56)	(2.49 ± 0.22, 0.34 ± 0.27, 2.56)
1FIG J1744.3–3051	PL	2.25 ± 0.18	2.51 ± 0.24	2.15 ± 0.21	2.33 ± 0.24
1FIG J1745.0–2905	LP	(2.08 ± 0.18, 0.94 ± 0.27, 2.54)	(2.23 ± 0.24, 1.07 ± 0.36, 2.54)	(1.97 ± 0.23, 1.08 ± 0.35, 2.54)	(2.28 ± 0.20, 0.85 ± 0.29, 2.54)
1FIG J1745.1–3012	LP	(2.75 ± 0.17, 0.18 ± 0.15, 0.45)	(3.10 ± 0.25, 0.08 ± 0.19, 0.45)	(2.67 ± 0.19, 0.22 ± 0.18, 0.45)	(2.90 ± 0.20, 0.11 ± 0.17, 0.45)
1FIG J1745.5–2859	LP	(2.28 ± 0.06, 0.21 ± 0.04, 2.69)	(2.33 ± 0.07, 0.22 ± 0.05, 2.69)	(2.28 ± 0.06, 0.21 ± 0.05, 2.69)	(2.30 ± 0.07, 0.21 ± 0.05, 2.69)
1FIG J1746.4–2843	LP	(2.66 ± 0.12, 0.19 ± 0.12, 3.12)	(2.73 ± 0.14, 0.22 ± 0.14, 3.12)	(2.65 ± 0.12, 0.21 ± 0.13, 3.12)	(2.69 ± 0.13, 0.20 ± 0.13, 3.12)
1FIG J1746.5–3240	LP	(2.26 ± 0.16, 0.82 ± 0.23, 2.12)	(2.49 ± 0.16, 0.71 ± 0.24, 2.12)	(2.22 ± 0.17, 0.84 ± 0.25, 2.12)	(2.40 ± 0.16, 0.73 ± 0.24, 2.12)
1FIG J1747.0–2826	LP	(2.58 ± 0.12, 0.00 ± 0.00, 0.33)	(2.83 ± 0.15, 0.00 ± 0.00, 0.33)	(2.57 ± 0.13, 0.00 ± 0.00, 0.33)	(2.71 ± 0.14, 0.00 ± 0.00, 0.33)
1FIG J1747.2–2959	LP	(2.51 ± 0.09, 0.54 ± 0.13, 2.35)	(2.65 ± 0.10, 0.57 ± 0.15, 2.35)	(2.48 ± 0.10, 0.59 ± 0.14, 2.35)	(2.67 ± 0.09, 0.50 ± 0.13, 2.35)
1FIG J1747.6–2442	LP	(3.03 ± 0.71, 1.39 ± 0.85, 0.93)	(3.06 ± 0.62, 0.87 ± 0.56, 0.93)	(2.99 ± 0.69, 1.36 ± 0.83, 0.93)	(3.05 ± 0.68, 1.19 ± 0.75, 0.93)
1FIG J1748.1–2449	LP	(2.45 ± 0.15, 1.16 ± 0.23, 2.42)	(2.64 ± 0.14, 0.86 ± 0.22, 2.42)	(2.46 ± 0.14, 1.15 ± 0.24, 2.42)	(2.58 ± 0.14, 0.97 ± 0.23, 2.42)
1FIG J1748.2–2856	LP	(2.40 ± 0.25, 0.43 ± 0.25, 2.54)	(2.65 ± 0.24, 0.39 ± 0.28, 2.54)	(2.45 ± 0.24, 0.43 ± 0.25, 2.54)	(2.59 ± 0.24, 0.39 ± 0.26, 2.54)
1FIG J1748.2–2816	LP	(2.38 ± 0.14, 1.03 ± 0.19, 0.41)	(2.57 ± 0.15, 0.89 ± 0.20, 0.41)	(2.42 ± 0.14, 1.01 ± 0.19, 0.41)	(2.49 ± 0.14, 0.91 ± 0.19, 0.41)
1FIG J1749.1–2917	LP	(2.20 ± 0.31, 0.57 ± 0.34, 2.31)	(2.47 ± 0.31, 0.56 ± 0.40, 2.31)	(2.07 ± 0.37, 0.69 ± 0.43, 2.31)	(2.25 ± 0.36, 0.68 ± 0.47, 2.31)
1FIG J1750.2–3705	PL	2.53 ± 0.21	2.57 ± 0.21	2.51 ± 0.20	2.56 ± 0.20
1FIG J1753.5–2931	LP	(2.26 ± 0.30, 0.49 ± 0.35, 2.29)	(2.53 ± 0.28, 0.40 ± 0.36, 2.29)	(2.03 ± 0.39, 0.62 ± 0.48, 2.29)	(2.28 ± 0.34, 0.49 ± 0.42, 2.29)
1FIG J1753.6–2539	LP	(2.36 ± 0.14, 0.54 ± 0.14, 0.46)	(2.59 ± 0.13, 0.35 ± 0.13, 0.46)	(2.39 ± 0.14, 0.53 ± 0.14, 0.46)	(2.51 ± 0.14, 0.41 ± 0.14, 0.46)
1FIG J1755.5–2511	LP	(2.09 ± 0.28, 0.72 ± 0.33, 2.89)	(2.72 ± 0.29, 0.56 ± 0.41, 2.89)	(2.08 ± 0.27, 0.73 ± 0.32, 2.89)	(2.47 ± 0.28, 0.58 ± 0.35, 2.89)
1FIG J1758.5–2405	LP	(2.23 ± 0.18, 0.23 ± 0.21, 0.36)	(2.48 ± 0.17, 0.17 ± 0.20, 0.36)	(2.20 ± 0.18, 0.22 ± 0.20, 0.36)	(2.41 ± 0.18, 0.14 ± 0.19, 0.36)
1FIG J1759.0–2345	LP	(1.96 ± 0.18, 0.24 ± 0.12, 0.34)	(2.19 ± 0.19, 0.17 ± 0.14, 0.34)	(2.01 ± 0.18, 0.22 ± 0.13, 0.34)	(2.03 ± 0.22, 0.22 ± 0.15, 0.34)
1FIG J1800.5–2359	LP	(2.46 ± 0.10, 0.19 ± 0.10, 0.46)	(2.57 ± 0.11, 0.12 ± 0.10, 0.46)	(2.47 ± 0.10, 0.18 ± 0.10, 0.46)	(2.50 ± 0.11, 0.14 ± 0.10, 0.46)
1FIG J1801.1–2313	LP	(3.42 ± 0.45, 1.70 ± 0.55, 3.02)	(4.13 ± 1.01, 2.24 ± 1.03, 3.02)	(3.48 ± 0.54, 1.76 ± 0.68, 3.02)	(3.82 ± 0.75, 2.02 ± 0.82, 3.02)

**Table 7**  
(Continued)

Name 1FIG	Type	Pulsars Intensity-scaled	Pulsars Index-scaled	OBstars Intensity-scaled	OBstars Index-scaled
1FIG J1801.2–2451	PL	$2.43 \pm 0.18$	$2.79 \pm 0.21$	$2.48 \pm 0.16$	$2.69 \pm 0.17$
1FIG J1801.4–2330	LP	$(3.27 \pm 1.06, 0.56 \pm 1.12, 3.10)$	$(2.89 \pm 0.19, 0.00 \pm 0.02, 3.10)$	$(3.27 \pm 0.65, 0.54 \pm 0.66, 3.10)$	$(2.90 \pm 0.21, 0.04 \pm 0.23, 3.10)$
1FIG J1801.6–2358	PL	$2.11 \pm 0.24$	$2.33 \pm 0.25$	$2.11 \pm 0.22$	$2.29 \pm 0.22$
1FIG J1802.2–3043	PL	$1.91 \pm 0.22$	$1.98 \pm 0.23$	$1.85 \pm 0.22$	$1.90 \pm 0.22$
1FIG J1808.2–3358	PL	$2.60 \pm 0.23$	$2.63 \pm 0.24$	$2.51 \pm 0.24$	$2.60 \pm 0.23$
1FIG J1809.5–2332	LP	$(2.66 \pm 0.04, 0.42 \pm 0.05, 0.32)$	$(2.69 \pm 0.04, 0.40 \pm 0.05, 0.32)$	$(2.66 \pm 0.04, 0.42 \pm 0.05, 0.32)$	$(2.68 \pm 0.04, 0.40 \pm 0.05, 0.32)$

**Notes.**

<sup>a</sup> Parameter tuple  $\alpha, \beta, E_b$  (GeV) for spectral model  $dN/dE \propto (E/E_b)^{-\alpha-\beta \log(E/E_b)}$ .

<sup>b</sup> Parameter  $\alpha$  for spectral model  $dN/dE \propto E^{-\alpha}$ .

## REFERENCES

- Abazajian, K. N., Canac, N., Horiuchi, S., & Kaplinghat, M. 2014, *PhRvD*, **90**, 023526
- Abazajian, K. N., & Kaplinghat, M. 2012, *PhRvD*, **86**, 083511
- Abdo, A. A., Ackermann, M., Ajello, M., et al. 2009a, *ApJ*, **703**, 1249
- Abdo, A. A., Ackermann, M., Ajello, M., et al. 2009b, *A&A*, **500**, 193
- Abdo, A. A., Ackermann, M., Ajello, M., et al. 2010a, *ApJS*, **188**, 405
- Abdo, A. A., Ackermann, M., Ajello, M., et al. 2010b, *ApJ*, **718**, 348
- Abdo, A. A., Ackermann, M., Ajello, M., et al. 2010c, *ApJ*, **710**, 133
- Abdo, A. A., Ackermann, M., Ajello, M., et al. 2011, *ApJ*, **734**, 116
- Abdo, A. A., Ackermann, M., Ajello, M., et al. 2012, *ApJ*, **758**, 140
- Abdo, A. A., Ajello, M., Allafort, A., et al. 2013, *ApJS*, **208**, 17
- Acero, F., et al. 2015a, *ApJ*, submitted
- Acero, F., Ackermann, M., Ajello, M., et al. 2015b, *ApJS*, **218**, 23
- Ackermann, M., Ajello, M., Albert, A., et al. 2012b, *ApJS*, **203**, 4
- Ackermann, M., Ajello, M., Atwood, W. B., et al. 2012a, *ApJ*, **750**, 3
- Ackermann, M., Ajello, M., Baldini, L., et al. 2011, *ApJ*, **726**, 81
- Ackermann, M., Albert, A., Atwood, W. B., et al. 2014, *ApJ*, **793**, 64
- Ackermann, M., et al. 2016, *ApJ*, in press
- Agrawal, P., Batell, B., Fox, P. J., & Harnik, R. 2015, *JCAP*, **5**, 11
- Aharonian, F., Akhperjanian, A. G., Bazer-Bachi, A. R., et al. 2006a, *Natur*, **439**, 695
- Aharonian, F., Akhperjanian, A. G., Bazer-Bachi, A. R., et al. 2006b, *ApJ*, **636**, 777
- Atwood, W. B., Abdo, A. A., Ackermann, M., et al. 2009, *ApJ*, **697**, 1071
- Bergström, L. 2000, *RPPh*, **63**, 793
- Bloemen, J. B. G. M., Dogiel, V. A., Dorman, V. L., & Ptuskin, V. S. 1993, *A&A*, **267**, 372
- Bloemen, J. B. G. M., Strong, A. W., Mayer-Hasselwander, H. A., et al. 1986, *A&A*, **154**, 25
- Bouchet, L., Strong, A. W., Porter, T. A., et al. 2011, *ApJ*, **739**, 29
- Breitschwerdt, D., Dogiel, V. A., & Völk, H. J. 2002, *A&A*, **385**, 216
- Bronfman, L., Casassus, S., May, J., & Nyman, L.-Å. 2000, *A&A*, **358**, 521
- Calore, F., Cholis, I., McCabe, C., & Weniger, C. 2015a, *PhRvD*, **91**, 063003
- Calore, F., Cholis, I., & Weniger, C. 2015b, *JCAP*, **3**, 38
- Castro, D., Slane, P., Carlton, A., & Figueroa-Feliciano, E. 2013, *ApJ*, **774**, 36
- Ciprini, S., et al. 2007, in *AIP Conf. Ser.* 921, *The First GLAST Symp.*, ed. S. Ritz, P. Michelson, & C. A. Meegan (Melville, NY: AIP), 546
- Damiani, F., Maggio, A., Micela, G., & Sciortino, S. 1997, *ApJ*, **483**, 350
- Daylan, T., Finkbeiner, D. P., Hooper, D., et al. 2014, arXiv:1402.6703
- Digel, S. W., Grenier, I. A., Hunter, S. D., Dame, T. M., & Thaddeus, P. 2001, *ApJ*, **555**, 12
- Dobler, G., Finkbeiner, D. P., Cholis, I., Slatyer, T., & Weiner, N. 2010, *ApJ*, **717**, 825
- Faucher-Giguère, C.-A., & Loeb, A. 2010, *JCAP*, **1**, 5
- Feng, J. L. 2010, *ARA&A*, **48**, 495
- Genzel, R., Eisenhauer, F., & Gillessen, S. 2010, *RvMP*, **82**, 3121
- Goodenough, L., & Hooper, D. 2009, arXiv:0910.2998
- Gordon, C., & Macías, O. 2013, *PhRvD*, **88**, 083521
- Górski, K. M., Hivon, E., Banday, A. J., et al. 2005, *ApJ*, **622**, 759
- Green, D. A. 2014, *BASI*, **42**, 47
- Hooper, D., & Goodenough, L. 2011, *PhLB*, **697**, 412
- Hooper, D., & Slatyer, T. R. 2013, *PDU*, **2**, 118
- Huang, W.-C., Urbano, A., & Xue, W. 2013, arXiv:1307.6862
- Hunter, S. D., Bertsch, D. L., Catelli, J. R., et al. 1997, *ApJ*, **481**, 205
- Jungman, G., Kamionkowski, M., & Griest, K. 1996, *PhR*, **267**, 195
- Kerr, M. 2010, PhD thesis, Univ. Washington
- Lande, J., Ackermann, M., Allafort, A., et al. 2012, *ApJ*, **756**, 5
- Manchester, R. N., Hobbs, G. B., Teoh, A., & Hobbs, M. 2005, *AJ*, **129**, 1993
- Mattox, J. R., Bertsch, D. L., Chiang, J., et al. 1996, *ApJ*, **461**, 396
- Mayer-Hasselwander, H. A., Bertsch, D. L., Dingus, B. L., et al. 1998, *A&A*, **335**, 161
- Moskalenko, I. V., & Strong, A. W. 1998, *ApJ*, **493**, 694
- Navarro, J. F., Frenk, C. S., & White, S. D. M. 1997, *ApJ*, **490**, 493
- Nolan, P. L., Abdo, A. A., Ackermann, M., et al. 2012, *ApJS*, **199**, 31
- Porter, T. A., Moskalenko, I. V., Strong, A. W., Orlando, E., & Bouchet, L. 2008, *ApJ*, **682**, 400
- Shibata, T., Honda, N., & Watanabe, J. 2007, *A&A*, **471**, 411
- Stecker, F. W., & Jones, F. C. 1977, *ApJ*, **217**, 843
- Story, S. A., Gonthier, P. L., & Harding, A. K. 2007, *ApJ*, **671**, 713
- Strong, A. W., Bloemen, J. B. G. M., Dame, T. M., et al. 1988, *A&A*, **207**, 1
- Strong, A. W., & Mattox, J. R. 1996, *A&A*, **308**, L21
- Su, M., Slatyer, T. R., & Finkbeiner, D. P. 2010, *ApJ*, **724**, 1044
- Tam, P. H. T., Kong, A. K. H., Hui, C. Y., et al. 2011, *ApJ*, **729**, 90
- Trotta, R., Jóhannesson, G., Moskalenko, I. V., et al. 2011, *ApJ*, **729**, 106
- Vladimirov, A. E., Jóhannesson, G., Moskalenko, I. V., & Porter, T. A. 2012, *ApJ*, **752**, 68
- Wolleben, M. 2007, *ApJ*, **664**, 349
- Yusifov, I., & Küçük, I. 2004, *A&A*, **422**, 545